Physics of Fluids ARTICLE pubs.aip.org/aip/pof

Assisted heat transfer enhancement in non-Newtonian dielectric fluids based on ion conduction phenomena

Cite as: Phys. Fluids **35**, 113109 (2023); doi: 10.1063/5.0174095
Submitted: 28 August 2023 · Accepted: 25 October 2023 ·
Published Online: 16 November 2023

Di-Lin Chen,[1,2] Kang Luo,[1,2] Chun Yang,[3] and Hong-Liang Yi[1,2,a)]

AFFILIATIONS

[1] School of Energy Science and Engineering, Harbin Institute of Technology, Harbin 150001, People's Republic of China
[2] Key Laboratory of Aerospace Thermophysics, Ministry of Industry and Information Technology, Harbin 150001, People's Republic of China
[3] School of Mechanical and Aerospace Engineering, Nanyang Technological University, 50 Nanyang Avenue, Singapore 639798

[a)] Author to whom correspondence should be addressed: yihongliang@hit.edu.cn

ABSTRACT

Electric field-assisted technologies show prospects for heat removal in electronic cooling scenarios with electro-thermo-convection phenomena. The coupled multiphysics field model is built using the finite volume method, and two configurations (depending upon the orientation of the electric field and gravity) are investigated for different shear-thinning properties and polymer elasticities. The results demonstrate a remarkable impact on the heat exchange efficiency, energy budget, plume morphology, and force distribution features. Two key partitions (buoyancy or Coulomb force-dominated regions) can be divided by Rayleigh number $Ra \leq 10^3$ and electric Reynolds number $Re_E \leq 1.57$. A heat transfer boost of 13.9 times and 5.0 times was obtained in the two arrangements vs no electric reinforcement. The shear-thinning shows a noticeable positive contribution, and the heat transfer efficiency can be modulated by polymer elasticity within a wide parameter range. A detailed evaluation of the interfacial forces reveals the nonmonotonic curves of fluid convection and energy inputs.

I. INTRODUCTION

The contemporary widespread usage of microelectronic devices in space and on earth puts new demands on both actively and passively enhanced means of heat transfer.[1,2] Compact electronic devices often suffer from the pending difficulties of high-level heat fluxes and local islands, and efficient thermal management has emerged as the key objective for the electronics industry. Electrohydrodynamics (EHD),[3] as a new controllable means of regulatory techniques, not only shows great potential for enhanced heat transfer but also plays an important role in the fields of actuated devices,[4,5] two-phase flow pumping,[6] electrostatic dedusting,[7] jet printing,[8,9] etc.

EHD technology, regarded as inducing the movement of dielectric fluids, is a discipline that studies the interaction between electrostatic forces and flow. EHD-related studies can be divided into three categories depending on the generation of free charges: injection,[10,11] induction,[12] and ionic conduction.[13] Each has its own advantages, drawbacks, and suitability for different industrial scenarios.[14] Compared to the former two mechanisms, the ionic conduction mechanism allows the pumping capacity to be effectively regulated by naturally occurring impurity molecules or additional added electrolytes. Over time, EHD has been applied in broad industrial scenarios due to its height adjustable, noiseless, and frictionless features,[12] as opposed to mechanically manipulated equipment. Numerous ion transport mechanisms and inducing flows in weakly dielectric fluids have been studied in experimental and numerical surveys. The reinforcing benefits of Coulomb force-induced electroconvection (EC) in liquid film boiling,[15,16] ion wind,[17,18] and two-phase pumping[6,19] have been proven, with accompanying quantification of the flow rate and pressure generation.[20–22] Several investigations have extended to electrode arrangements[23] and particle image velocity (PIV) measurements, dealing with the different electrode pairs and field-enhanced dissociation effects (Onsager–Wien effect).[21,24] Furthermore, versatile flow distribution[25,26] has been demonstrated to modulate direction and mass rate in an active and passive manner. Different types of microscale tests[17,27,28] indicated possible implementations in aerospace and micro/flexible components.

In the context of heat exchange enhancement based on EHD techniques [also known as electro-thermo-convection (ETC)], Singhal *et al.*[29] have reported an induced flow circulation for cooling microprocessors. Nourdanesh *et al.*[30] examined the average velocity, electrode current, and pumping efficiency of free-surface liquid films at different thicknesses and temperatures under optimum operating conditions. Golsefid *et al.*[31] determined the fitting electrode configuration for enhanced ETC in a rectangular enclosure. In addition, the new Joule heating imposed in the control volume shows a dominant effect at low Reynolds numbers. Wang *et al.*[32] also obtained the heat removal effect in a hot sink with two symmetrical evanescent fins with EHD reinforcement. The average convective heat transfer coefficient can be increased by a factor of 3.5 compared to natural convection conditions. Not long ago, Jafari *et al.*[1] experimentally assessed the heat transfer manifestations of ionic conduction pumping with two types of dielectric liquid films. The higher the ionic mobility ratio and operating temperature are, the lower the density/viscosity, thus increasing the removed heat flux.

Although the aforementioned ETC surveys cover an extensive experimental scenario, the uniqueness of numerical simulations lies in a deeper insight into the multiphysics field coupling with the driving mechanism and heat reinforcement. EHD conduction has shown abundant flow phenomena in numerical investigations with various geometrical configurations, including single cylindrical electrodes,[33] three cylinders,[34] coplanar electrodes,[35] flush electrodes,[36] and planar electrodes.[37] In terms of exploring physical aspects, the first prediction[13,38] of the characteristic thickness of DSLs (heterocharge layers or dissociation layers) has been resolved. The Onsager–Wien effect has been used to explain some numerical deviations that do not match experimental settings.[24,39] Two limiting operations of EHD conduction pumping have also been represented by Ohmic and saturation regimes.[40] The literature review reveals that ETC, driven by Coulomb forces and buoyancy, is a frontier scientific problem of widespread interest in EHD perspectives. Due to the highly complex coupling of multiple physical fields, ETCs display abundant flow phenomena that have not yet been widely investigated. Additionally, the dual action implemented for coupling thermal buoyancy with Coulomb forces is not well understood.

Foreseeably, the nature of fluid properties has a substantial influence on the flow pattern and dynamic properties in engineering. Relevant theories are not fully established, and the mechanism exploration is still at a preliminary stage with diverse rheological phenomena. Most of the available reports on ETC relate to Newtonian fluids.[1,30–33] Whereas having apparent relevance to industrial applications, to our knowledge, there are no published accounts of ETC problems in non-Newtonian fluids.[41–43] Non-Newtonian properties are more universal; for example, some silicone oils, greases, polymer solutions in industry, blood and organism fluids in animals, salt solutions, and molten polymers are non-Newtonian fluids. In certain defined circumstances, Newtonian fluids may also have non-Newtonian properties, such as shear-thinning,[44] extrusion expansion,[45] and rod climbing effects.[46] Most literature related to non-Newtonian properties has been widely discussed in various contexts, such as electroosmotic flow,[47] turbulent drag reduction,[48,49] Li-cells and stable electrodeposition,[50,51] and electroelastic instability.[52,53] In the realm of EHD, the insightful aspects of non-Newtonian rheological properties have been considered in liquid film flow,[54] pressure-electro-osmotic dual driving systems,[55] Rayleigh–Bénard convection,[56] jet printing,[57] electrothermal transport,[58] nonlinear bifurcation,[59] etc. Hence, our study is motivated by two main aspects. First, the non-Newtonian ETC problem indicates promising prospects for active heat transfer enhancement in microdevices, which facilitates expansion to diversified fluid media and industrial scopes. Second, it is also conducive to deepening the knowledge construction of EHD and thermophysics. The ETC problem of non-Newtonian properties belongs to the unexplored and innovative frontier, with a broader correlation to our daily life.

Despite the presence of several efforts to perform non-Newtonian flows with rheological properties, ETC problems have not been addressed for targeting the complex implementation of temperature–Coulomb force–viscous forces–fluid flow and polymer elasticity. In this chapter, we investigate the ETC problem in non-Newtonian weakly dielectric liquids, extending the enhanced heat transfer capability in two configurations. The set of electro-thermo-convection equations is implemented in our direct numerical simulation (DNS) by a finite volume approach. The physical mechanisms associated with heat transfer are then elucidated. Next, we depict the ETC program for viscoelastic dielectric fluids with corresponding dimensionless governing equations in Sec. II. Boundary constraints and numerical implementation are displayed in Sec. III. The heat transfer performances assisted by the electric field are presented in Sec. IV, and we conclude in Sec. V by summarizing the relevant key findings.

II. PROBLEM STATEMENT

The ionic conduction-enhanced ETC of parallel plate structures is shown in Fig. 1 with two configurations. We consider an enhanced heat transfer program with high-temperature hot chips located at the bottom. The height between the two planes is d, with a computational width of $3d$. Equally sized heat chips ($0.4d$) are assumed to be located at the bottom center in both configurations with a cold wall on the upper surface, creating upward natural convective plumes due to the

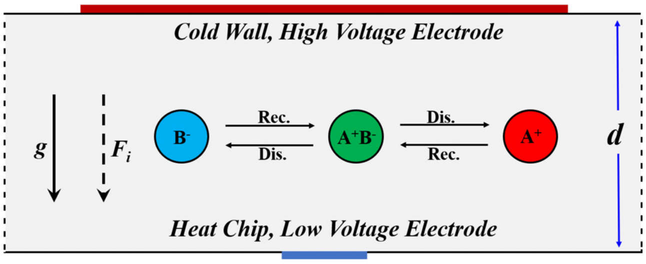

(a) Config. 1

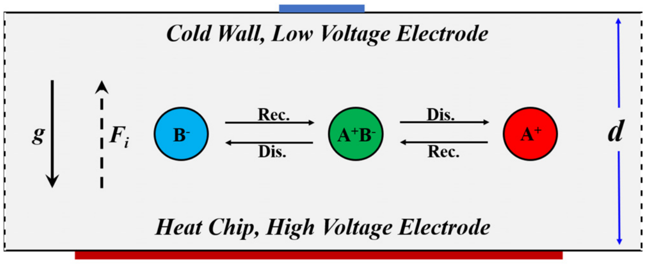

(b) Config. 2

FIG. 1. Geometrical configuration of electro-thermo-convection: (a) Config. 1: gravity **g** in the same direction as the net Coulomb-inducing F_i; (b) Config. 2: gravity **g** is reversed with F_i.

thermal buoyancy forces. Config. 1 has the direction of gravity **g** in the same direction as the net Coulomb-inducing F_i.[38,40,60] Config. 2 shows that gravity is reversed with F_i. In general, EHD conduction devices are designed with asymmetric electrodes, where positive and negative charges migrate toward the opposite polarity electrodes in response to the electric field **E**, resulting in differential thickness DSLs, which create a combined Coulomb force to produce a net flow in the desired direction.[38] Therefore, the heat transport and dynamic properties in relation to electro-thermo-convection (ECT) are investigated in Secs. III and IV with two configurations.

A. Hydrodynamic, energy, and electric equations

The hydrodynamic, energy, and electric equations are mainly regarded to depict the ETC system in our setting. The Navier–Stokes equations consider thermal buoyancy forces, non-Newtonian additional stresses, and Coulombic driving forces. Furthermore, because the current in the dielectric liquid is so modest, electromagnetic impacts and Joule heating can be ignored,[59,61] and the flow satisfies the Boussinesq approximation. By considering the aforementioned hypotheses, the subsequent list of governing equations can be determined:

$$\rho_m\left(\frac{\partial \mathbf{u}}{\partial t} + \mathbf{u}\cdot\nabla\mathbf{u}\right) = -\nabla p + 2\eta_s\nabla\cdot\mathbf{D} + \nabla\cdot\boldsymbol{\tau} + \rho_E\mathbf{E} + \rho_m\delta\mathbf{g}(\theta-\theta_{ref}), \tag{1}$$

$$\nabla\cdot\mathbf{u} = 0, \tag{2}$$

$$\frac{\partial\theta}{\partial t} + \mathbf{u}\cdot\nabla\theta = a\nabla^2\theta, \tag{3}$$

$$\mathbf{E} = -\nabla\phi, \tag{4}$$

$$\nabla\cdot(\varepsilon\nabla\phi) = -\rho_E, \tag{5}$$

where $\mathbf{u}$, p, $\rho_E = e_0(z_+c_+ + z_-c_-)$, $z_\pm$, $c_\pm$ and e are the fluid velocity, pressure, space charge density, ionic valence, concentration, and elementary charge, respectively. η_s is the solvent dynamic viscosity, and $\mathbf{D} = \frac{1}{2}[\nabla\mathbf{u} + (\nabla\mathbf{u})^T]$ is the ratio of the deformation tensor. $\boldsymbol{\tau}$ is the non-Newtonian polymeric stress tensor described by different constitutive models. $\mathbf{g} = (0, -g)$ is the gravitational acceleration, θ_{ref} is the reference temperature, and δ is the thermal expansion coefficient. θ is the temperature, and a is the thermal diffusivity. ϕ is the voltage, $\mathbf{E}$ is the electric field, $\varepsilon = \varepsilon_r\varepsilon_0$ is the fluid permittivity, and ε_0 is the vacuum permittivity.

B. Ion dissociation-recombination

Next, we need to explore the ion generation and transport conservation conditions.[62] Dissociation and recombination of neutral substance concentration c_0 are regarded as a charge source in the ionic conduction mechanism. The common reaction process can be described[40,63] as follows:

$$AB \overset{dis}{\underset{rec}{\rightleftarrows}} A^+ + B^-, \tag{6}$$

where AB is generally a naturally soluble neutral species or an externally added electrolyte. A^+ and B^- are cations and anions dissociated from the neutral substances. Applying an electric field, the electroneutral equilibrium of the bulk volume is disturbed, which results in the formation of DSLs (heterocharge layers or dissociation layers) in the vicinity of the electrodes, with a thickness:[3,37,40]

$$\lambda_H \approx \frac{\varepsilon K E_0}{\sigma}, \tag{7}$$

where K, ε, and σ are the ionic mobility, fluid permittivity, and fluid conductivity, respectively. E_0 is the field amplitude perpendicular to the electrode plane. The λ_H dimension relies upon the fluid nature and imposed electric field.

Notably, an external field strength is far from producing ion injection from nonflat surfaces or electrode tips[37] in the ion conduction mechanism. The reaction equilibrium (reversible) for a neutral species (c_0) within a dielectric fluid can be expressed as

$$k_D c_0 = k_R c_+^{eq} c_-^{eq} = k_R (c^{eq})^2, \tag{8}$$

where c_+^{eq} and c_-^{eq} stand for the concentrations of dissolved anions and cations at an equilibrium state. k_D and k_R denote the dissociation and recombination rates, respectively, at which the reaction occurs.

The Onsager–Wien effect has been reported to explain the deviation between experimental and numerical results.[40,64] With an applied external electric field, the dissociation rate of neutral substances is noticeably higher than the ionic recombination rate in DSLs. The correlation with the electric field **E** is

$$k_D(|\mathbf{E}|) = k_D^0 F(b), \tag{9}$$

where k_D^0 refers to the dissociation rate at thermodynamic equilibrium in the absence of an electric field. $F(b) = I_1(4b)/2b$ is known as the Onsager function, and b represents the enhanced dissociation rate factor. I_1 is the modified Bessel function of the first kind and order 1. b can be calculated by $b = l_B/l_o$, with the Bjerrum distance and the Onsager distance:[40,63]

$$l_B = e_0^2/4\pi\varepsilon k_B T, \quad l_o = \sqrt{e_0/4\pi\varepsilon|\mathbf{E}|}. \tag{10}$$

To further simplify the EHD conduction problem, both anions and cations are given equivalent mobilities ($K_+ = K_- = K, D_+ = D_- = D$). The recombination rates reveal a $k_R = 2e_0K/\varepsilon$ relationship for liquid properties depending on Langevin's approximation. The altered Nernst–Planck equation of ion transport follows the form

$$\frac{\partial c_\pm}{\partial t} + \nabla\cdot(\mathbf{u}c_\pm + z_\pm c_\pm K\mathbf{E} - D\nabla c_\pm) = \frac{2e_0Kc_0^2}{\varepsilon}\left(F(b) - \frac{c_+c_-}{c_0^2}\right). \tag{11}$$

The left-hand side presents the time derivative, ion convection, ion migration, and ion diffusion. The right-hand side characterizes the discrepancy between ion dissociation and ion recombination.

C. Non-Newtonian Giesekus model

Briefly, the non-Newtonian polymeric stress tensor $\boldsymbol{\tau}$ in Navier–Stokes equations is related to the conformational tensor,

$$\boldsymbol{\tau} = \frac{\eta_p}{\lambda}(\mathbf{C} - \mathbf{I}), \tag{12}$$

where η_p is the polymeric viscosity coefficient and λ is the relaxation time. λ denotes the characteristic scale for polymer molecules to recover to their initial equilibrium state after being deformed by a perturbation. Based on the above definition, the conformation tensor is symmetric positive definite (SPD) and is equal to the identity matrix $\boldsymbol{I}$ when the polymers are in the equilibrium state, which guarantees the realization of the log-conformation reformulation (LCR)[65] that will be introduced later.

Although the intrinsic form of the conformational tensor depends on different viscoelastic constitutive models (determined by semiempirical and theoretical methods), its generalized form is

$$\frac{\partial \mathbf{C}}{\partial t} + \mathbf{u}\cdot\nabla\mathbf{C} - \left(\mathbf{C}\cdot\nabla\mathbf{u}^T + \nabla\mathbf{u}\cdot\mathbf{C}\right) = -\frac{1}{\lambda}g(\mathbf{C}), \tag{13}$$

where function $g(\mathbf{C})$ is specified by the selected model. For example, the Oldroyd-B model describes the relation $g(\mathbf{C}) = \mathbf{C} - \mathbf{I}$. Nevertheless, the introduction of a maximum elongation in FENE-type models may lead to numerical collapse if the trajectories of the conformational tensor are beyond the threshold.[66] More stable constitutive forms are alternative options. Both the Phan–Thien–Tanner (PTT) and Giesekus models are useful for recognizing the shear-thinning and viscoelasticity of polymer fluids. The PTT model consists of more parameters for recovering the complex properties of the material; however, this poses difficulties for data analysis. Therefore, the Giesekus model is adopted in the present study with a single parameter, which helps distinguish the shear-thinning and elasticity effects,[67–69] making it suitable for concentrated polymer solutions. In addition, a quadratic form of the stress is incorporated into the model $g(\mathbf{C}) = \alpha\mathbf{C}^2 + (1-2\alpha)\mathbf{C} - (1-\alpha)\mathbf{I}$, which allows for cross-polymer interactions. The evolution of the Giesekus conformation tensor is

$$\begin{aligned}\frac{\partial \mathbf{C}}{\partial t} + \mathbf{u}\cdot\nabla\mathbf{C} - \left(\mathbf{C}\cdot\nabla\mathbf{u}^T + \nabla\mathbf{u}\cdot\mathbf{C}\right)\\ = -\frac{1}{\lambda}\left[\alpha\mathbf{C}^2 + (1-2\alpha)\mathbf{C} - (1-\alpha)\mathbf{I}\right].\end{aligned} \tag{14}$$

The parameter α in Eq. (13) is a mobility factor, and the term containing α has been attributed to anisotropic Brownian motion or anisotropic hydrodynamic drag on the constituent polymer molecules.[70] It is required that $0 \leq \alpha \leq 0.5$, as discussed in Refs. 69 and 71. Setting $\alpha = 0$ changes the format to a typical Oldroyd-B model. Giesekus studied the sensitivity in some simple viscometric flows and showed the ability of the model to characterize the following viscoelastic features:[69] shear-thinning, nonvanishing first and second normal stress differences, extensional viscosity with finite asymptotic value, nonexponential stress relaxation, and startup curves. The properties in simple shear are also investigated to demonstrate its accuracy in predicting stress overshoot, which fits well with experimental observations.

D. Dimensionless governing equations

The equations and results in this paper are dimensionless in terms of the following quantities:

$$\begin{gathered} x, y \sim d \quad c_\pm \sim c_0, \qquad E \sim E_0, \\ \phi \sim (\phi_1 - \phi_0), \quad \theta \sim (\theta_{hot} - \theta_{cold}) \\ u \sim KE_0, \quad t \sim d/KE_0 \sim d^2/K(\phi_1 - \phi_0), \\ P \sim \rho_m K^2 E_0^2. \end{gathered} \tag{15}$$

Therefore, the set of dimensionless control equations involved are as follows (labeled with $*$):

$$\begin{aligned}\frac{\partial \mathbf{u}^*}{\partial t^*} + \mathbf{u}^*\cdot\nabla\mathbf{u}^* = -\nabla p^* + \frac{\beta}{Re_E}\nabla^2\mathbf{u}^* + \frac{1-\beta}{Wi\cdot Re_E}\nabla\cdot\mathbf{C}\\ + C_0 M^2\left(c_+^* - c_-^*\right)\mathbf{E}^* + \frac{Ra}{Pr}\theta^*,\end{aligned} \tag{16}$$

$$\nabla\cdot\mathbf{u}^* = 0, \tag{17}$$

$$\frac{\partial \theta^*}{\partial t^*} + \mathbf{u}^*\cdot\nabla\theta^* = \frac{1}{Pr}\nabla^2\theta^*, \tag{18}$$

$$\frac{\partial c_\pm^*}{\partial t^*} + \nabla\cdot\left(c_\pm^*\left(\mathbf{u}^* \pm \mathbf{E}^*\right)\right) - \gamma\nabla^2 c_\pm^* = 2C_0\Big(F\big(b(|\mathbf{E}^*|)\big) - c_+^* c_-^*\Big), \tag{19}$$

$$\nabla^2\phi^* = -C_0\left(c_+^* - c_-^*\right), \tag{20}$$

$$\mathbf{E}^* = -\nabla\phi^*, \tag{21}$$

$$\begin{aligned}\frac{\partial \mathbf{C}}{\partial t^*} + \mathbf{u}^*\cdot\nabla\mathbf{C} = \mathbf{C}\cdot\nabla\mathbf{u}^* + \mathbf{C}\cdot\left(\nabla\mathbf{u}^*\right)^T\\ - \frac{1}{Wi}\left[\alpha\mathbf{C}^2 + (1-2\alpha)\mathbf{C} - (1-\alpha)\mathbf{I}\right].\end{aligned} \tag{22}$$

The dimensionless numbers in the above equations are summarized as

$$\begin{gathered} C_0 = \frac{e c^{eq,0} d}{\varepsilon E_0}, \quad \gamma = \frac{k_B T}{e_0 E_0 d}, \quad Re_E = \frac{\rho_m K E_0 d}{\eta_0}, \\ M = \frac{\sqrt{\varepsilon/\rho_m}}{K}, \quad Wi = \frac{\lambda u_0}{d}, \quad \beta = \frac{\eta_s}{\eta_s + \eta_p}, \\ Ra = \frac{\rho_m g\delta(\theta_{hot} - \theta_{cold})d^3}{\eta_0}, \quad Pr = \frac{\nu}{a}. \end{gathered} \tag{23}$$

The conduction number C_0 characterizes a ratio of two typical times, the ion transport time $t_K = d/KE_0$ and the Ohmic time $t_\sigma^0 = \varepsilon/\sigma_0$, and it is a key parameter for distinguishing the two limiting states in the EHD conduction phenomenon.[37,40] The diffusion number γ is the ratio of the thermal electric field ($E_T = k_B T/e_0 d$) to the imposed electric field (E_0). Re_E (electric Reynolds number) represents the ratio between the Coulomb force and the viscous force, determined by the speed of ion migration ($u = KE_0$). M is defined as the ratio of hydrodynamic mobility to ionic mobility. The Weissenberg number Wi describes a measurement of the polymer relaxation time with respect to the system timescale, and β is known as the viscosity ratio between solvent viscosity and total viscosity. The Rayleigh number Ra identifies the ratio of the buoyancy force to the viscous force, and the Prandtl number Pr indicates the ratio of momentum diffusivity to thermal diffusivity. For the sake of simplicity, superscripts $*$ are omitted in subsequent chapters.

III. BOUNDARY CONDITIONS AND NUMERICAL IMPLEMENTATION

Based on Fig. 1, we consider a program for EHD-enhanced heat transfer with high-temperature hot chips located at the bottom with two electrode configurations. The boundary constraints on each boundary for the governing equations (15)–(22) are summarized in Table I. The bottom center is setup as a hot chip with a constant temperature, and the bottom rest is considered adiabatic. The lateral left and right borders are considered to be symmetric, which is suitable for the spacing of the heat slices that are long enough in the x-direction. We also summarize the fluid properties and thermal parameters used

TABLE I. Boundary conditions in two configurations.

Region	Computational boundaries
Config. 1	
L.V electrode/hot chip	$c_- = 0, n\cdot\nabla c_+ = 0, \phi = 0, \mathbf{u} = 0, \theta = 1$
H.V electrode/cold wall	$c_+ = 0, n\cdot\nabla c_- = 0, \phi = 1, \mathbf{u} = 0, \theta = 0$
Top wall	$n\cdot\nabla c_+ = 0, n\cdot\nabla c_- = 0, \mathbf{u} = 0, n\cdot\nabla\phi = 0, \theta = 0$
Bottom wall	$n\cdot\nabla c_+ = 0, n\cdot\nabla c_- = 0, \mathbf{u} = 0, n\cdot\nabla\phi = 0, n\cdot\nabla\theta = 0$
Left and right	Symmetry
Config. 2	
H.V electrode/hot chip	$c_+ = 0, n\cdot\nabla c_- = 0, \phi = 1, \mathbf{u} = 0, \theta = 1$
L.V electrode/cold wall	$c_- = 0, n\cdot\nabla c_+ = 0, \phi = 0, \mathbf{u} = 0, \theta = 0$
Top wall	$n\cdot\nabla c_+ = 0, n\cdot\nabla c_- = 0, \mathbf{u} = 0, n\cdot\nabla\phi = 0, \theta = 0$
Bottom wall	$n\cdot\nabla c_+ = 0, n\cdot\nabla c_- = 0, \mathbf{u} = 0, n\cdot\nabla\phi = 0, n\cdot\nabla\theta = 0$
Left and right	Symmetry

for dodecane in Table II, which is a dielectric fluid widely implemented in industry and has been validated by several experiments and numerical simulations.[33,35,72] Suppose polymer polyisobutylene (PIB) is added to the dodecane to form a viscoelastic fluid in our letter.

The numerical iterative process of non-Newtonian fluid flows often involves the high Weissenberg number problem (HWNP),[65,73] in which the use of the log-conformation reformulation (LCR) method has been implemented. A new variable $\mathbf{\Psi}$ is introduced, defined as the matrix logarithm of the conformation tensor $\mathbf{C}$,

$$\mathbf{\Psi} = \log(\mathbf{C}) = \mathbf{R}^T \log(\mathbf{\Lambda})\mathbf{R}. \tag{24}$$

Above, $\mathbf{R}$ is an orthogonal matrix composed of the eigenvectors of $\mathbf{C}$, and $\mathbf{\Lambda}$ is a diagonal matrix whose diagonal elements are the eigenvalues of $\mathbf{C}$. Equation (13) of the conformation tensor is reformatted as

$$\begin{aligned}\frac{\partial\mathbf{\Psi}}{\partial\tilde{t}} &+ \tilde{\mathbf{u}}\cdot\nabla\mathbf{\Psi} - (\mathbf{\Omega}\cdot\mathbf{\Psi} - \mathbf{\Psi}\cdot\mathbf{\Omega}) - 2\mathbf{B}\\ &= -\frac{1}{Wi}\mathbf{R}\left[\alpha\mathbf{\Lambda} + (1-2\alpha)I - (1-\alpha)\mathbf{\Lambda}^{-1}\right]\mathbf{R}^T,\end{aligned} \tag{25}$$

where $\mathbf{B}$ is a symmetric traceless matrix and $\mathbf{\Omega}$ is an anti-symmetric matrix. Thus, the conformational tensor $\mathbf{C}$ can be recovered by $\mathbf{\Psi}$ as

$$\mathbf{C} = \exp(\mathbf{\Psi}). \tag{26}$$

The LCR has the advantage of eliminating the deviation between the polynomial fitting of the tensor $\mathbf{C}$ and the exponentially changing curve. The non-Newtonian ETC problem we studied cannot be derived analytically due to the strongly nonlinear nature of the control equations. For stability and efficiency, the numerical study is performed via the finite volume method (FVM) in the open-source OpenFOAM® toolbox. Furthermore, details of the numerical implementation and some verification cases can be found in our previous publications[62,63] and will not be repeated here. The benchmark validates the ion conduction mechanism in a line-plate structure with fitting curves of the experimental data[33] in Appendix A (Fig. 13). The Giesekus model is specified with the parameters of weak elasticity $Wi = 10^{-4}$, viscosity ratio $\beta = 0.98$, and $\alpha = 10^{-3}$. Relevant curves show that the peak velocities of the Newtonian model are in high agreement with the predictions of the Giesekus model, with minor errors of no more than 5%. Grid-independent verification using a finer mesh in electrode regions to capture DSLs with the total mesh numbers $M1 = 88\,800$, $M2 = 125\,000$, and $M3 = 150\,000$. Three grids are available to satisfy the demands of solving the fluid flow and ion transport accurately, with M2 serving as the option in our numerical implementation.

IV. RESULTS AND DISCUSSION

The effect of enhanced heat transfer by the electric field is highlighted in Secs. IV A–IV C with two configurations (Config. 1—F_i in the same direction as gravity and Config. 2—F_i in the opposite direction as gravity), as well as the influence of the non-Newtonian properties on the heat transfer. The wide range parameters of $10^1 \leqslant Ra \leqslant 10^5$ and $0 \leqslant Re_E \leqslant 8$ are the predominant driving forces that regulate the thermal buoyancy and electric field strength. For ease of analysis, the other dimensionless parameters are set to $Pr = 21.15$, $M = 55$, $\gamma = 5\times10^{-6}$, and $C_0 = 59$ unless noted specifically. C_0 is a prominent parameter that distinguishes the operating regimes of the ionic conduction flow, and the relevant details can be found in Appendix B.

Below, we analyze the flow regimes of pure natural convection and EHD flow in Sec. IV A. We also demonstrate the natural convection profile and ETC performance enhanced by electric fields in Sec. IV B. The heat transfer and flow properties with the addition of polymers are investigated in Sec. IV C. Polymer elasticity is tuned by the dimensionless Weissenberg number and viscosity ratio β. Then, the mobility factor α in the Giesekus model is used to modulate the shear-thinning properties.

TABLE II. Thermophysical and dielectric properties of dodecane.

Parameters	Value (unit)	Parameters	Value (unit)
Elementary charge, e_0	1.6022×10^{-19} (C)	Ionic mobility, K	$2.81\times10^{-9}\,[\mathrm{m^2/(s\cdot V)}]$
Boltzmann constant, k_B	1.3806×10^{-23} (J/K)	Ionic diffusivity, D	$7.16\times10^{-11}\,(\mathrm{m^2/s})$
Density, ρ_m	749.5 $(\mathrm{kg/m^3})$	Specific heat capacity, C_p	2.21 (kJ/kg · K)
Dynamic viscosity, η_0	1.34×10^{-3} (Pa · s)	Thermal conductivity, k	0.140 (W/m · K)
Relative permittivity, ε_r	2	Thermal expansion, δ	7.8×10^{-4} (1/K)
Temperature, θ_{ref}	275 (K)	Electrical conductivity, σ_0	2.96×10^{-8} S/m

A. Natural convection alone and EHD-induced flow

The basic flow patterns of EHD conduction flow and pure natural convection are discussed in this section. The anisotropic effect $\alpha = 0.01$, maximum $Wi = 1 \times 10^{-3}$, and viscosity ratio $\beta = 0.98$ are maintained to strongly approximate the Newtonian properties in the Giesekus model. Figure 2 illustrates the flow patterns induced by full natural convection ($Ra = 10^1$–10^5, with Re_E=0) and the EHD conduction mechanism (Re_E= 0.8–8, with $Ra = 0$). Under pure Rayleigh–Bénard convection (RBC) conditions, Fig. 2(a) shows the thermal plume formed on the surface of the hot chip, which becomes more integrated as the Ra number increases, gradually forming a mushroom-like morphology with a stalk. Two counterrotating flow units are formed in Fig. 2(b), and the higher the Ra number is, the higher the maximum velocity is concentrated in the central region with an upwards jet. In ECF induced by pure conduction mechanisms, two electrode arrangements will produce differences in the net Coulomb force direction, thus changing the pumping orientation with flexible active manipulation capabilities.[38,60] In our setup, the net charge density distribution and streamlines for two different configurations are shown in Fig. 2(c) and Fig. 2(d), and F_i represents the direction of the main flow induced by the net Coulomb force.[5,24,26] In both configurations, four main vortex pairs are shaped. As Re_E increases, the sizing pattern of the mainstream and secondary vortices changes on the symmetrical centerline. Under Config. 1, the F_i direction is accompanied by the main vortex pointing downwards toward the ground electrode in Fig. 2(c). However, F_i is associated with the main vortex pointing upwards toward the high voltage electrode in Fig. 2(d).

The velocity and temperature profiles along the center of the x-direction for the two configurations are displayed in Fig. 3. In Figs. 3(a) and 3(b), the spike-like velocity curves become more pronounced, matching the contour map in Fig. 2(b). The emergence of a spike-like velocity distribution demonstrates that the thermal convective effect outweighs the diffusion effect. For $Ra \geq 10^3$, the steep gradient at the center marks a thermal plume structure with a high-temperature jet to the upper cold wall. The strong thermal convective effect induced a radical gradient shift, as shown in Fig. 3(b). In the pure EC scenario, both configurations reveal the presence of a double-hump distribution in Figs. 3(c) and 3(d). Distinctive features are the inverted double-hump structure in both configurations, demonstrating a shift orientation F_i dominated by the net Coulomb force. In addition, the U_y magnitude tends to increase monotonically with increasing Re_E in Figs. 3(c) and 3(d), indicative of an increased input power, translated into kinetic energy within the flow field.[63] In summary, we compared full EC flow and RBC flow with two configurations in terms of net charge density, flow direction, plume morphology, temperature, and velocity contours, thus facilitating a fundamental understanding for Sec. IV B.

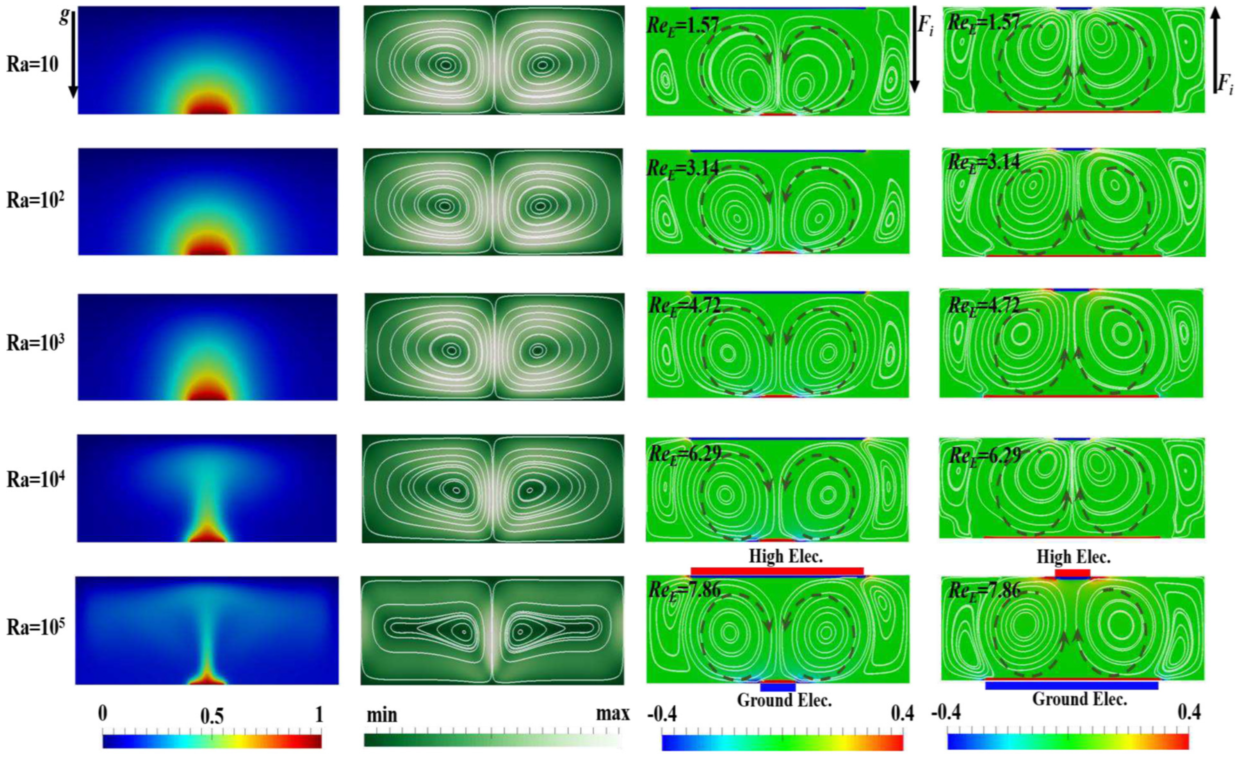

(a) Temperature, RBC, Re_E=0 (b) Velocity, RBC, Re_E=0 (c) Net charge density-1, EC, Ra=0 (d) Net charge density-2, EC, Ra=0

FIG. 2. Natural convection in pure form and EHD-induced flow characteristics. (a) Temperature field, pure RBC, Re_E=0. (b) Velocity field-imposed streamlines, pure RBC, Re_E=0. (c) Contour map of net charge density-imposed streamlines, Pure EC, configuration 1, Ra =0. (d) Contour map of net charge density-imposed streamlines, Pure EC, configuration 2, Ra =0.

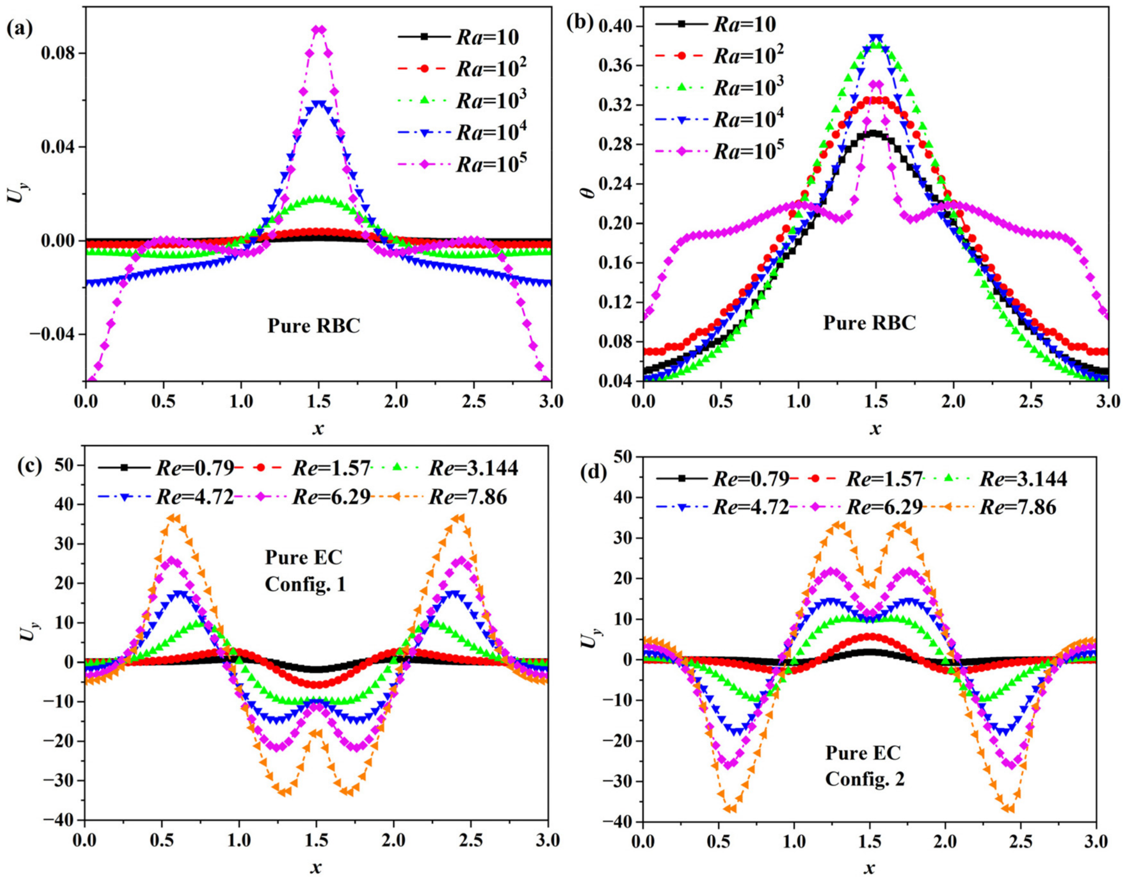

FIG. 3. Temperature and velocity distributions of pure natural convection and EHD-induced flow along the middle horizontal line in the *x* direction. (a) Velocity distribution of pure RBCs. (b) Temperature distribution of pure RBCs. (c) Velocity distribution of pure EC with ConFIG. 1. (d) Velocity distribution of pure EC with Config. 2.

B. Heat transfer performance in two configurations

The electro-thermo-convection (ETC) patterns enhanced by the EHD conduction mechanism in the two configurations are shown in Fig. 4, with a constant $Ra = 10^3$. Apparently, the EHD-enhanced thermal plume morphology was significantly altered in Figs. 4(a) and 4(c) compared with pure RBCs. In particular, the originally well-defined plume structure in Fig. 2(a) disappears and is replaced by pair symmetric cells under Config. 1. There are two reasons to explain this phenomenon. First, the net Coulomb driving flow is downward due to the electric field, thus suppressing the buoyancy force effect (upward). On the other hand, the flow field carrying the heat quantity tends to be homogeneous in the *x*-direction dominated by EC, resulting in a pair of thermal cells. With increasing Re_E, the velocity field exhibits a central vortex that increases in Figs. 4(c) and 4(d), with the corner vortices moving toward the small asymmetric electrodes. The net Coulomb force F_i is upward in Fig. 4(c). Although the full thermal plume is still shown in Fig. 4(c), the top temperature field gradually tends to be spiky as Re_E increases. The spiky profile indicates that the driving forces are much greater at the center than at the ends, entraining the heat flux to be ejected upward before the temperature diffusion produces its effect. At the left and right sides of the hot chip, the induced ECF is pointing toward its center without carrying heat out of the volume.

Sequentially, we also give the temperature and velocity profiles in the centerline. Config. 1 shows a homogeneous *x*-directional temperature with increasing Re_E in Fig. 5(a). Figure 5(c) shows a decreasing rootstock refinement heat plume in Config. 2 as Re_E increases. The discrepancy in temperature profiles from pure RBCs is due to the highly EC-induced symmetrical dual vortex patterns and driving force. In the velocity profile, compared to the previous pure EC trends shown in Figs. 3(c) and 3(d), there is still a double-hump pattern with changing flow amplitude. We have demonstrated the impacts of temperature and velocity profiles in a cooperative RBC-EC system. The relevant results undoubtedly have a deep influence on the heat transfer performance, which will be clarified later.

To elucidate the enhanced heat transfer efficiency of ETC, we defined the Nusselt number on the hot chip and the corresponding ratio of the EHD enhanced heat transfer R_{ht} as follows:

$$Nu = \frac{L}{S_{block}(T_{hot} - T_{cold})} \int_S \left. \frac{\partial T}{\partial n} \right|_{hot} dS, \qquad R_{ht} = \frac{Nu}{Nu_0}, \tag{27}$$

where T_{hot}, T_{cold}, and S represent the temperature of the hot chip, the cold wall temperature of the upper surface, and the area of the hot chip, respectively. Nu_0 refers to the Nusselt number for pure RBCs

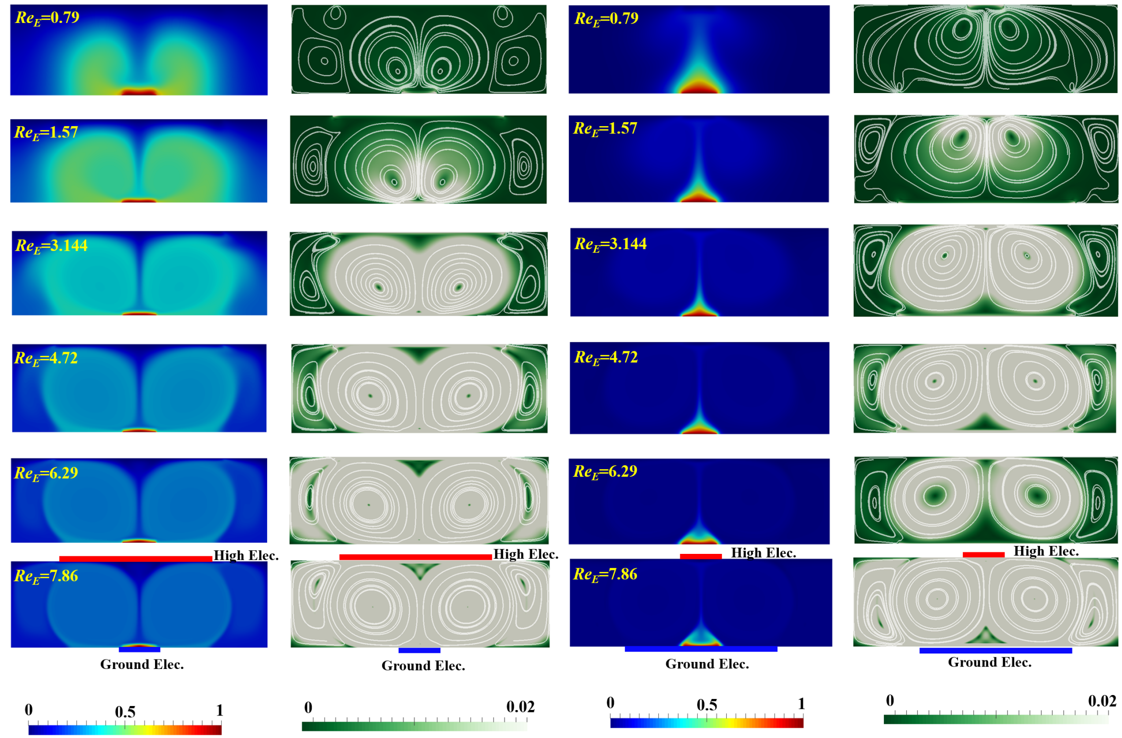

(a) Temperature, RBC-EC, Config.1 (b) Velocity, RBC-EC, Config.1 (c) Temperature, RBC-EC, Config.2 (d) Velocity, RBC-EC, Config.2

FIG. 4. Electro-thermo-convection pattern enhanced by ionic conduction in two configurations, with a constant $Ra = 10^3$. (a) Temperature distribution for Config. 1; (b) velocity distribution for Config. 1 imposed streamlines; (c) temperature distribution for Config. 2; (d) velocity distribution for Config. 2 imposed streamlines.

without the aid of an electric field. Furthermore, we define the L^2—norm[63] of the velocity field—kinetic energy E_k:

$$E_k = \frac{1}{2V_t}\int |\mathbf{u}|^2 dV = \frac{1}{2V_t}\sum_{k=1}^{N} |\mathbf{u}_k|^2 V_k = \frac{1}{2N}\sum_{k=1}^{N} |\mathbf{u}_k|^2, \tag{28}$$

where V_k is the unit mesh volume with $V_t = NV_k$ and N is the number of grids. Accordingly, the elastic energy is given here as

$$E_p = \frac{1}{2V_t}\int \frac{\lambda}{\eta_p} tr(\boldsymbol{\tau}) dV = \frac{1}{2V_t}\sum_{k=1}^{N} \frac{\lambda}{\eta_p} tr(\boldsymbol{\tau}_\mathbf{k}) V_k = \frac{1}{2N}\frac{\lambda}{\eta_p}\sum_{k=1}^{N} tr(\boldsymbol{\tau}_\mathbf{k}). \tag{29}$$

The influence of the Rayleigh number Ra and the electrical Reynolds number Re_E on the heat transfer strength Nu for two configurations ($Ra = 10^3$) are illustrated in Fig. 6. Under typical RBC conditions in Fig. 6(a), the heat transfer is small at $Ra < 10^3$, determined by thermal diffusion. At $Ra > 10^3$, the heat transfer intensity sharply increases, and Nu increases by a factor of 4 compared to $Ra = 10$. In Config. 1 of Fig. 6(b), Nu displays an approximately linear relationship with Re_E. Due to the low-level contribution of Ra, EC flow-dominated heat transfer is shown. With Config. 2 in Fig. 6(c), Nu first linearly increases, reaching saturation between $Re_E = 3$–6.5, after which it continues to reinforce heat transfer. The Coulombic forces carried the heat rate upward against the cold wall, and the two ends of the hot chip were squeezed by the EC flow, resulting in a thinner thermal boundary layer.[41] A comparison with the U_y in Fig. 4(d) demonstrates that the offset created by the secondary vortices [the double-hump pattern in Fig. 5(d)], leading to an amplitude on the chip, serves to explain the heat saturation intensification. The other reason may be due to the emergence of saturation regimes for the EHD ion conduction mechanism, with no more ion dissociation occurring.[1,40,62] Furthermore, the insets in graphs (a)–(c) reveal the full thermal plume and even the needlelike morphology and the dominant role played by the EC-dominated ETC pattern at both ends of the chip in enhancing heat transfer. In particular, the golden dotted lines are shown in Fig. 6(c), indicating the double-hump velocity distribution and the alteration of the EC secondary flow, which results in the saturation effect of the heat transfer strength in some Re_E parameters. In addition, the time evolution Nu and E_k are given in Appendix A (Fig. 14). The larger Re_E is, the longer it takes to reach steady state compared to pure RBCs, which is consistent with most previous numerical predictions.[41,57,62] E_k shows an enhancement of one to two orders of magnitude compared to pure RBCs, indicating a significant EC role in providing an energy source for the flow field.

Above, we have demonstrated that an increasing Re_E has a profound effect on the heat transfer. In light of the above analysis, the heat transfer Nu over a wide range parameter is needed, as displayed in Fig. 7. In Fig. 7(a) of Config. 1, two significant partitions can be divided by the Rayleigh number Ra, namely, the thermal diffusion-dominated region ($Ra \leq 10^3$) and the thermal convection-dominated region ($Ra > 10^3$). In $Ra \leq 10^3$ cases, Nu depends on the EC magnitude due

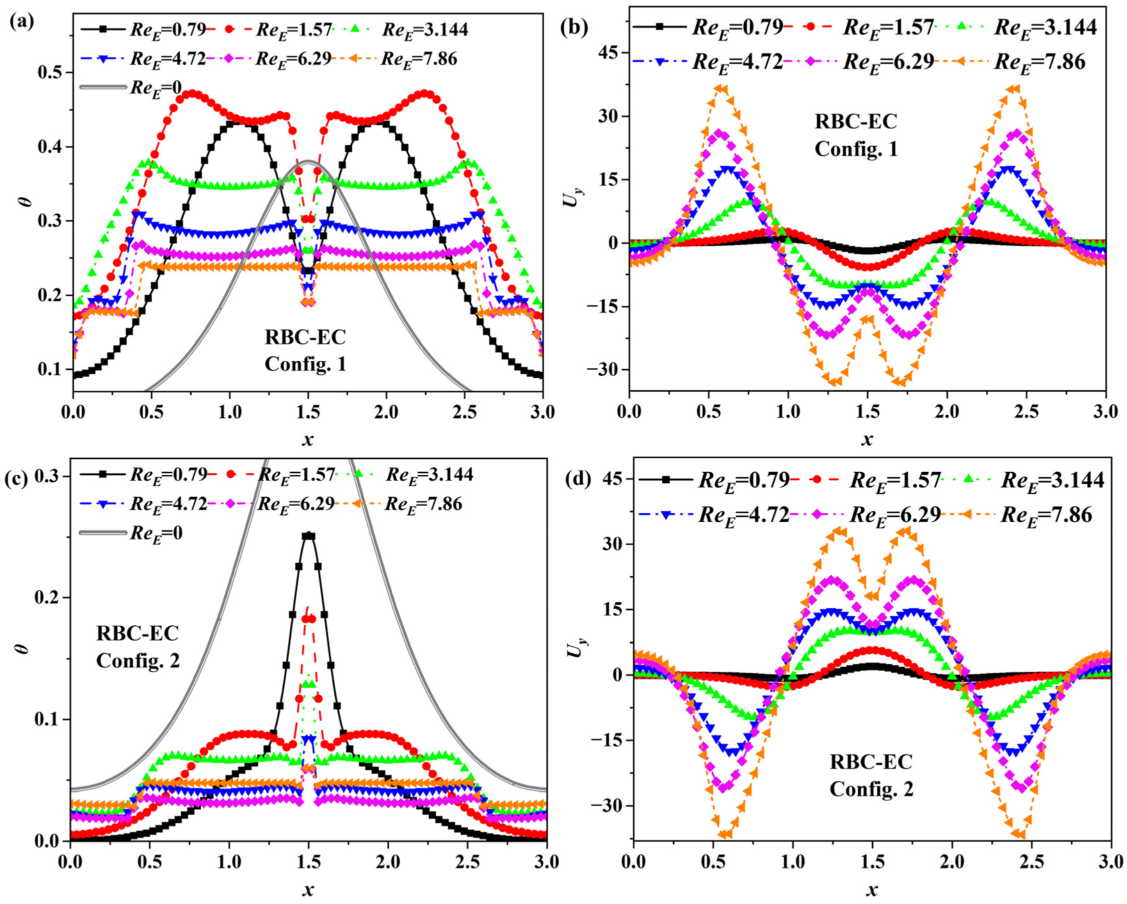

FIG. 5. Temperature vs velocity distribution of the RBC-EC system on the centerline, with a constant $Ra = 10^3$. (a) Config. 1, temperature field; (b) Config. 1, velocity field; (c) Config. 2, temperature field; (d) Config. 2, velocity field.

to extremely weak buoyancy force action. For a weak Coulombic driving force $Re_E < 1.57$ and $Ra \leq 10^3$, the heat transfer strength does not increase significantly, as shown in the inset of Fig. 7(a). The *Nu* relationship is similar to the phenomenon in Fig. 6(c), where *Nu* proceeds through a linear increase, saturation, and a secondary rise for Config. 2. At higher *Ra* numbers ($Ra = 10^4$ and 10^5) in Fig. 7(b), *Nu* is markedly stronger in the linear domain than in other *Ra* cases, reflecting the highly synergistic RBCs assisted by EC. In contrast, at high $Re_E > 6.29$, the whole system is dominated by EC-induced flow, and the heat transfer capacity tends to a uniformly high value of 7.8.

Obviously, the relevant results of Config. 2 do not exactly match the results reported by Selvakumar *et al.*[72] (the higher Re_E is, the higher *Nu* is accompanied by an increase in the maximum velocity) in Fig. 7 due to the different conduction numbers C_0 in this paper. Furthermore, the EHD conduction flow also increases the heat transfer for all Rayleigh numbers except the robust thermal buoyancy effect ($Ra = 10^4$ and 10^5). In Config. 1, R_{ht} is enhanced at low Rayleigh numbers, with the maximum $R_{ht} = 13.9$ higher without electric field reinforcement [Fig. 7(c)]. Under low Re_E and high *Ra*, the electroforce is too weak to induce a significant enhancement of heat transfer. With Config. 2, R_{ht} can reach a maximum of 5.02 times without the EHD reinforcement [Fig. 7(d)]. At higher *Ra*, the electric field enhancement is marginal, with R_{ht} reaching only 1.33 over a wide range of Re_E. Overall, Config. 1 (F_i in the same direction as gravity) allows higher heat transfer compared to Config. 2 (F_i in the opposite direction as gravity), and the heat exchange capacity in both arrangements is profoundly influenced by the EHD conduction mechanism.

To address the investigation of flow and heat transfer mechanisms, we compare the magnitude of Coulomb force $\rho_E E_y$ and the moment contribution of buoyancy force $\rho_m \delta \mathbf{g}(\theta - \theta_{ref}) e_y$ in the *y*-direction. Figure 8 illustrates the two limiting cases for $Ra = 10^1$ and $Ra = 10^5$. In comparison of the near-wall Coulomb force distributions, both display an increasing order with Re_E and do not differ in amplitude. The large values are mainly concentrated within the DSLs, with an appearing electroneutral bulk. This indicates that the energy input to the plume thermal boundary layer from the Coulomb force is equivalent. Observing the buoyancy force profiles, the large buoyancy effect $Ra = 10^5$ covers the whole plume structure for $Re_E < 3.144$. Thereby, revealing that the buoyancy force predominates the flow distribution ($Ra = 10^5$, $Re_E < 3.144$), an agreement with the results (buoyancy-led regions) in Figs. 7(a) and 7(c) is achieved.

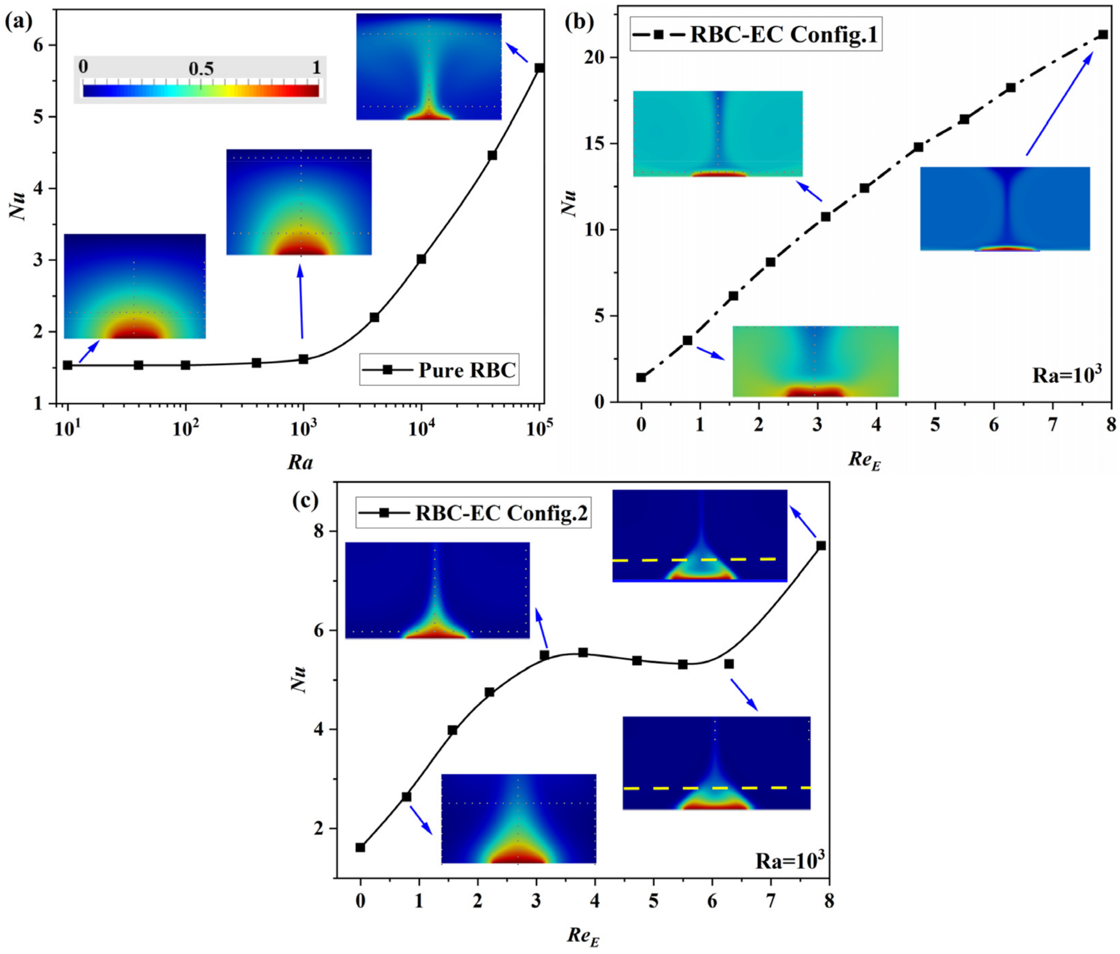

FIG. 6. The dependence of the heat transfer *Nu* number on the driving force. (a) *Ra* and *Nu* correlation in pure RBCs. (b) Re_E and *Nu* correlation in Config. 1 with a constant $Ra = 10^3$. (c) Re_E and *Nu* correlation in Config. 2 with a constant $Ra = 10^3$.

C. Influence of shear-thinning and polymer elasticity on heat transfer

As mentioned earlier, although they have apparent relevance to industrial applications, there are no published accounts of ETC problems in non-Newtonian fluids.[41–43] Dielectric fluids, which are commonly found in industry, will result in viscosity alterations that are noticeable with increasing shear rates. In addition, the utilization of low-conductivity liquids, such as refrigerants and transformer oils, is widespread in industry. By considering the rheological influence of polymer additions, it is possible to modulate flow rates and power remarkably, serving adjustable pumping and field-enhanced heat transfer scenarios in space and on land.[63] In Sec. II C, we outlined the Giesekus model for characterizing properties such as shear-thinning and nonvanishing first and second normal stresses. There is an exploration of rheological properties in ETC problems, including the incorporation of elastic dependence and shear-thinning effects. We will regulate the anisotropic effect α (0–0.5) to discuss different mobility factors on heat transfer and dynamic properties, with the fixed parameters $Wi = 0.1$, $\beta = 0.8$, $Re_E = 1.57$, and $Ra = 10^3$.

The cross-sectional temperature is shown in Fig. 9. With Config. 1, although the temperature remains similar to the double-hump distribution in Fig. 5(a), the temperature is more homogeneous on both sides of the hot chip, with a rising α parameter. The temperature profiles are due to the structure of the main vortex (Mv) and secondary vortex (Sv) of the EC, as shown in Appendix A (Figs. 15 and 16). The center offsets are also shown in Fig. 9(a) for the location and size of the Mv/Sv. Moreover, the U_y amplitudes tend to be higher with increasing α parameters, resulting in a remarkable reinforcement, as shown in Appendix A (Fig. 17). For Config. 2, the spiked thermal plume becomes narrower but covers a larger area as the α parameter increases in Fig. 9(b), indicating the shift of Sv toward the corners with the larger size of Mv. Furthermore, the heat transfer *Nu* subjected to shear-thinning effects is shown in Fig. 9(c). A sharp surge is induced at $\alpha < 0.1$ and a lesser enhancement in heat transfer intensity at $\alpha \geq 0.1$. The average kinetic energy curve in the inset also reveals the favorable influence of the shear-thinning function on the flow velocity and kinetic energy gains. The construction of Fig. 9 in terms of the energy mechanism[66] follows:

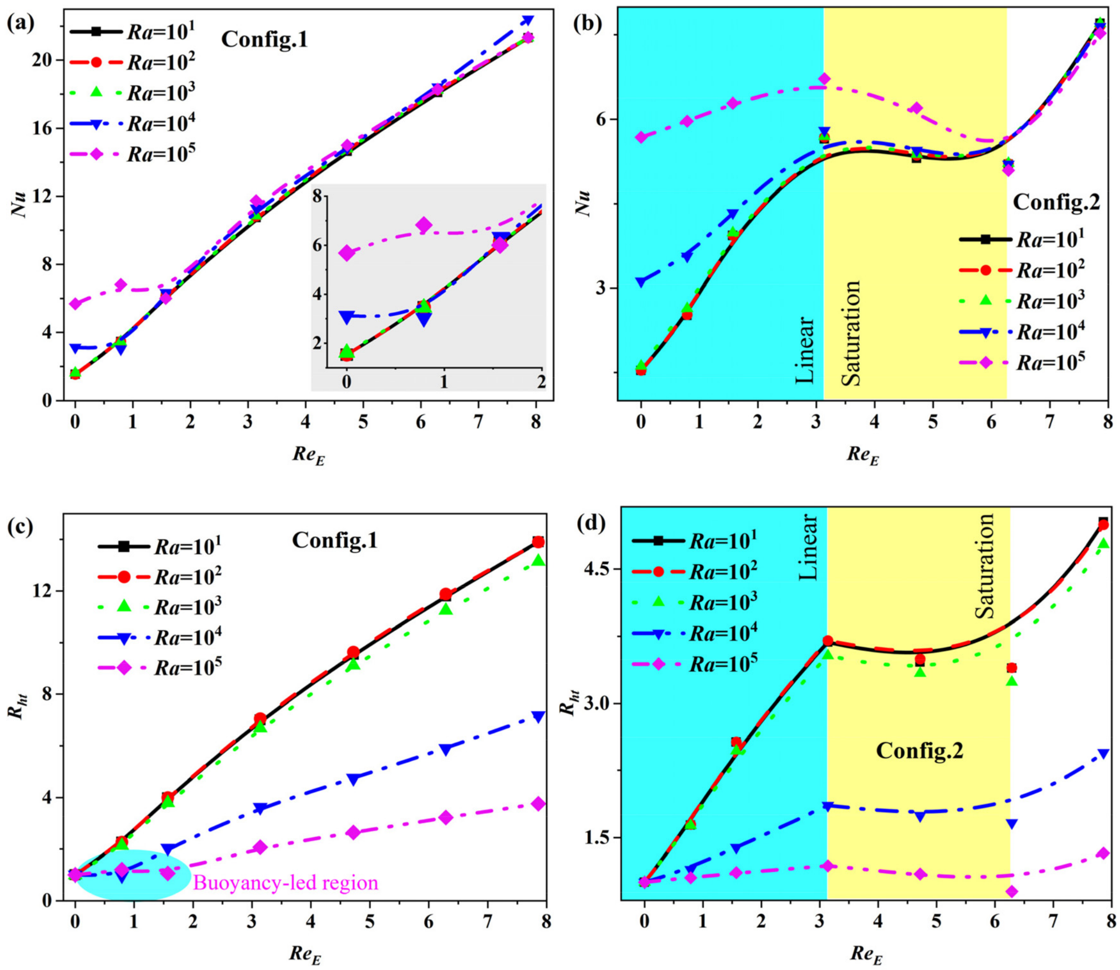

FIG. 7. The heat transfer *Nu* tends over a wide range of parameters at $10^1 \leqslant Ra \leqslant 10^5$ and $0 \leqslant Re_E \leqslant 8$. (a) Re_E and *Nu* correlation in Config. 1. (b) Re_E and *Nu* correlation in Config. 2. (c) Ratio of the EHD-enhanced heat transfer R_{ht} in Config. 1. (d) Ratio of the EHD-enhanced heat transfer R_{ht} in Config. 2.

First, the Coulombic forces dominate the flow state for Re_E=1.57 and $Ra = 10^3$ (compare the streamlines in Fig. 2, the pure EC resembles a direction-flipped symmetric pattern with two configurations). Second, the kinetic energy gains mainly from the electrical input, and the contributions of the thermal buoyancy forces are subtle. Third, the effect of polymer elastic energy is small due to the fixed elastic effect $Wi = 0.1$, $\beta = 0.8$, and diffusion in the closed system essentially accounts for two orders of magnitude less than other terms.[66,74] Hence, the remaining energy is converted into viscous dissipation of the whole system. The *Nu* discrepancy is due to the difference in EC patterns on the hot chip. From the analysis in Sec. II, the electroconvection above the hot chip is stronger at Config. 1, leading to a larger *Nu* number growth in Fig. 9(c). The inset shows the average kinetic energy in both configurations, where the two curves are highly coincident with no more than 2% deviation. Collectively, the relevant results demonstrate the positive promotion role of the vortex pattern and shear-thinning in ETC systems.

Next, to facilitate an analysis, Weissenberg numbers will be scanned within a broad range to discuss polymer elasticity effects, with other fixed sets $\alpha = 0.1$, $\beta = 0.8$, Re_E=1.57, and $Ra = 10^3$. The heat transfer strength *Nu* on the hot chip is displayed in Fig. 10. The arrows in Fig. 10(a) refer to the value for the Newtonian fluid scenario without polymer addition. R_{Nu} represents the ratio of the viscoelastic fluid Nu_V to the Newtonian flow Nu_0 in Fig. 10(b), $R_{Nu} = Nu_V/Nu_0$. *Nu* shows a 10% reduction (Config. 1) and a 5.5% reduction (Config. 2) in Fig. 10(a), respectively, with the polymer added initially. For weak elasticity $Wi < 0.1$, *Nu* displays a maximum reduction of up to 14% as *Wi* increases. One can interpret that the polymer absorbs kinetic energy from the flow field at low *Wi* numbers, resulting in a local reduction of the flow strength (kinetic energy).[66,74] When surpassing the threshold $Wi_{cr} = 0.01$, *Nu* exhibits a rising stage, suggesting the recovery of kinetic energy, which can be explained by polymer molecular relaxation at high elasticity, releasing elastic energy into the flow field.[62,63,74] In conjunction with the ratio R_{Nu} in Fig. 10(b), $R_{Nu} = 1$ denotes the absence of polymer addition. The vortex patterns of ETC-induced flow differ in the two configurations for almost equivalent energy input; however, the two curves have similar trends. The R_{Nu} can be modulated by polymer

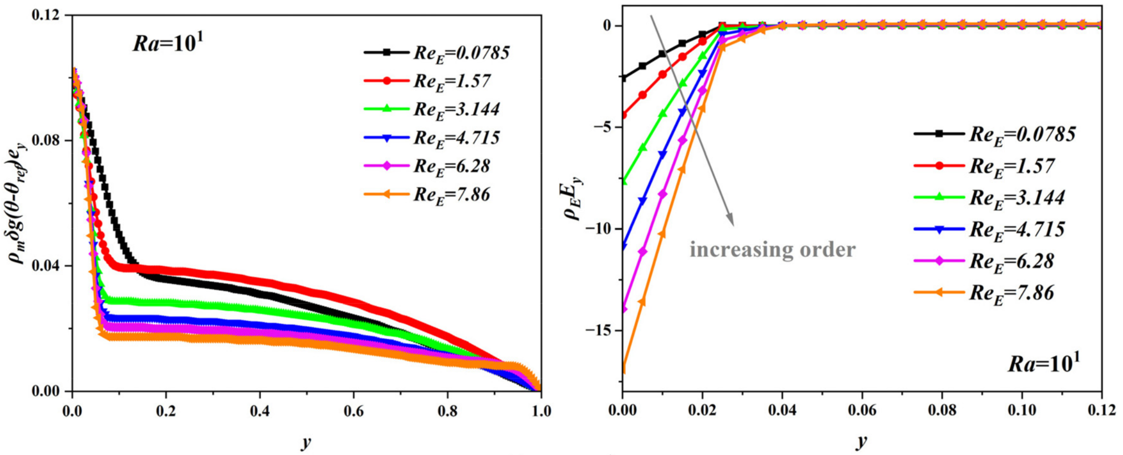

(a) Ra=10^1

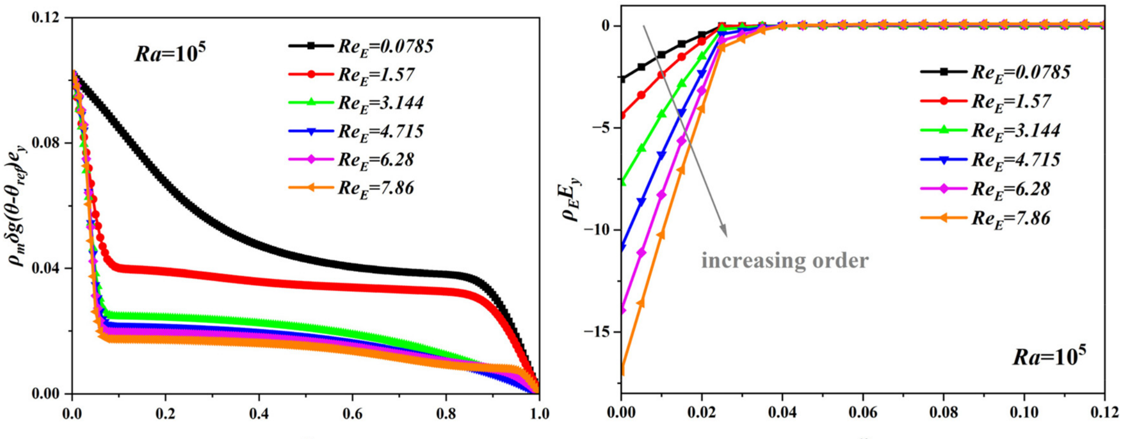

(b) Ra=10^5

FIG. 8. Coulomb force and buoyancy distribution of near-heat chips with (a) $Ra = 10^1$ and (b) $Ra = 10^5$.

elasticity in a range of 14.5% (Config. 1), while it is only influenced within a range of 11% (Config. 2).

Due to the asymmetric arrangement of the electrodes oriented horizontally and the hot chip in the bottom plate in Fig. 1, both the electric strength and the buoyancy force act mainly in the *y*-direction of the ETC. To visualize the mechanism behind the flow and heat transfer efficiency, we use the momentum equation in the vertical *y*-direction:

$$\rho_m\left(\frac{\partial u_y}{\partial t}+u_y\frac{\partial u_y}{\partial y}+u_x\frac{\partial u_y}{\partial x}\right)=-\frac{\partial p}{\partial y}+\eta_s\left(\frac{\partial^2 u_x}{\partial y^2}+\frac{\partial^2 u_y}{\partial x^2}\right)+\left(\frac{\partial \tau_{yy}}{\partial y}+\frac{\partial \tau_{xy}}{\partial x}\right)+\rho_E E_y+\rho_m\delta\mathbf{g}(\theta-\theta_{ref})e_y. \tag{30}$$

The left-hand side $\rho_m\left(\frac{\partial u_y}{\partial t}+u_y\frac{\partial u_y}{\partial y}+u_x\frac{\partial u_y}{\partial x}\right)$ reflects the momentum increment per unit volume of fluid per unit time, where $\rho_m\left(u_y\frac{\partial u_y}{\partial y}+u_x\frac{\partial u_y}{\partial x}\right)$ represents the acceleration due to the inhomogeneity of the flow field, also known as the convective term; $-\frac{\partial p}{\partial y}$ represents the pressure acting on the volume element; $\eta_s\left(\frac{\partial^2 u_x}{\partial y^2}+\frac{\partial^2 u_y}{\partial x^2}\right)$ represents the component of the viscous force term; $\left(\frac{\partial \tau_{yy}}{\partial y}+\frac{\partial \tau_{xy}}{\partial x}\right)$ represents the component of the elastic force in the *y*-direction; and $\rho_E E_y$ is the *y*-component of the Coulomb force. $\rho_m\delta\mathbf{g}(\theta-\theta_{ref})e_y$ is the buoyant force in the vertical direction.

In Fig. 11, we demonstrate the force distribution features at the interface. The effect of the polymer on the Coulomb force is shown in the inset of Fig. 11(a), close to the hot chips. The weak distinction is caused by interfacial ion transport, with ion convection, migration, and diffusion, where ion migration predominates in the EHD conduction mechanism. The main source of the buoyancy contribution shown in Fig. 11(b) is derived from the temperature variance of thermal convection. Although polymer influences are weak, there is significant variation in the near-chip region. In contrast to other factors, fluid convection is the underlying cause of the change in heat transfer capacity, as shown in Fig. 11(c), accompanied by the plume

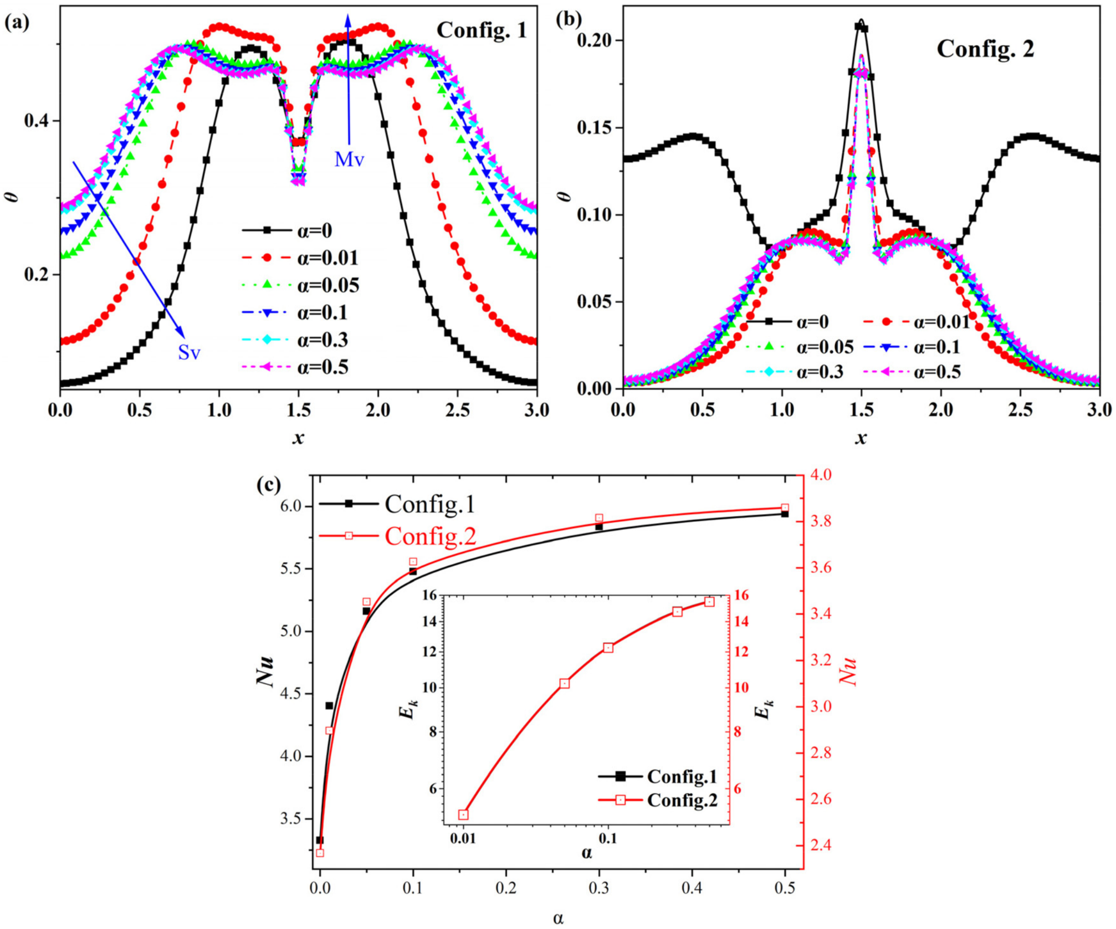

FIG. 9. Variation in the temperature distribution and heat transfer *Nu* subject to the shear-thinning effect. (a) Temperature of Config. 1; (b) Temperature of Config. 2; (c) The *Nu* curve, and the inset shows kinetic energy shifts.

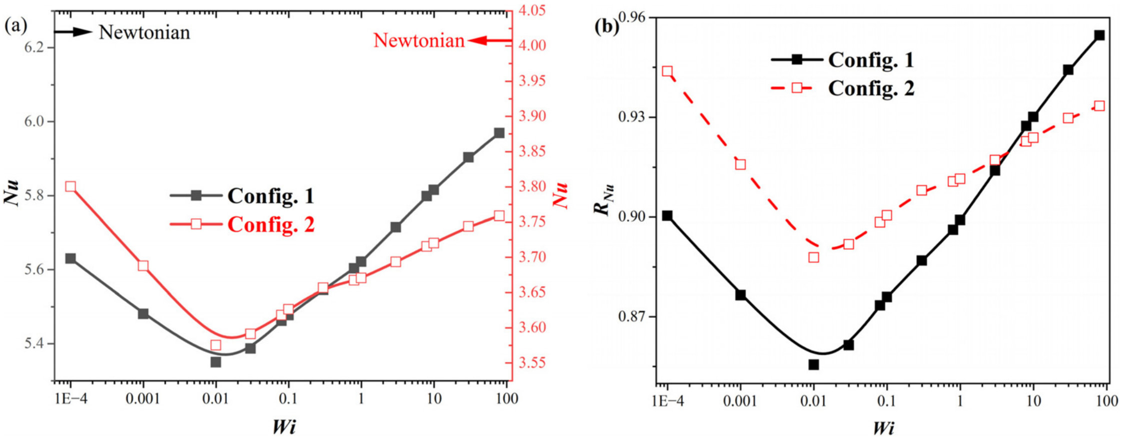

FIG. 10. The influence of polymer elasticity on heat transfer strength. (a) *Nu* vs Weissenberg number for two configurations and (b) heat ratio R_{Nu} of the polymer elasticity effect.

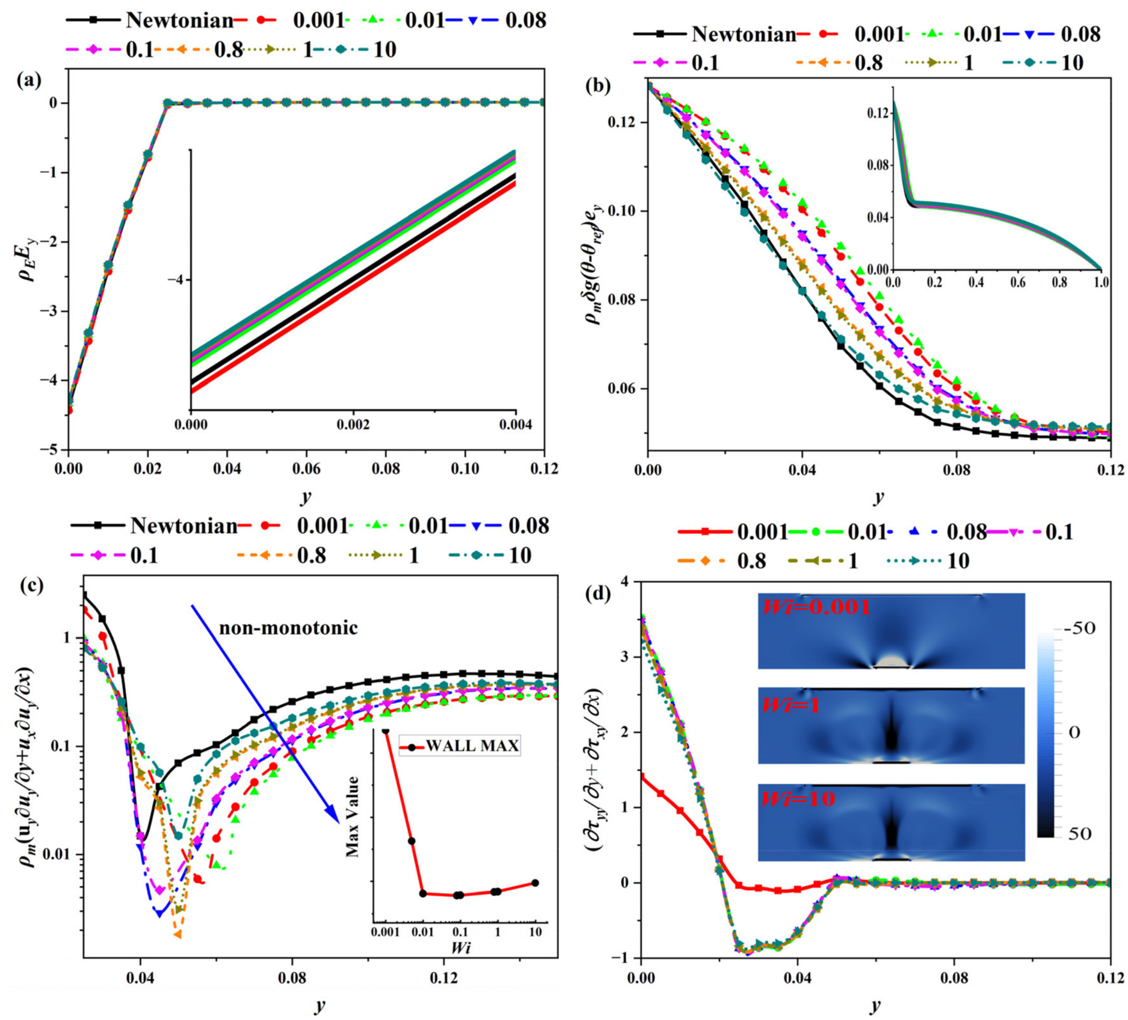

FIG. 11. Forces distribution near the interface characterizing the polymer elastic influence. (a) Coulomb force; (b) buoyancy force; (c) convective contribution; and (d) elastic stress. The fixed Re_E=1.57 and Ra =10^3.

morphology and the nonmonotonic nature of *Nu*. The convective strength as a function of *Wi* shown in the inset of Fig. 11(c) coincides with the heat transfer trend in Fig. 10(a).

The role of elastic forces in the momentum equation cannot be neglected due to the incorporation of polymers. Figure 11(d) displays the elastic force distribution, mainly focused on the nonzero values in the DSL altering the local flow pattern and energy budget. In general, the difference in the first normal stress difference ($N1 = \tau_{yy} - \tau_{xx}$) of the viscoelastic molecule is responsible for the turning of the flow regime, and we also show N_1 distributions in the insert of Fig. 11(d). N_1 from weak elasticity $Wi = 0.001$ displays homogenization in the solving domain. However, it displays high values in the center thermal plume jet with high polymer elasticity. The shape and magnitude differ very little between $Wi = 1$ and $Wi = 10$, which is consistent with the elastic energy E_p ($E_p = \frac{1}{2V_t}\int \frac{\lambda}{\eta_p} tr(\tau)dV$) feature shown in Fig. 12. The elastic interaction of the polymer molecules, with the absorption and release of the resultant elastic energy, which alters the fluid circulation and convection intensities in the localized flow area, is the fundamental factor responsible for the altered heat transfer capacity. Hence, we also show the global trend of the elastic energy E_p and E_k in Fig. 12. One can interpret that the polymer absorbs kinetic energy from the flow field at low *Wi* numbers, resulting in a local reduction of the flow strength (kinetic energy).[66,74] The plot (U_{max} vs *Wi*) shown in Appendix A (Fig. 17) also confirms the evolution of E_k. When surpassing the threshold $Wi_{cr} = 0.01$, *Nu* exhibits a rising stage, suggesting the recovery of kinetic energy, which can be explained by polymer molecular relaxation at high elasticity, releasing elastic energy into the flow field.[62,63,74] In overview, we illustrate the positive contribution of shear-thinning effects and the role of polymer microstructures in ETC systems that can serve the applications of thermal management devices with complex fluid properties.

V. CONCLUSIONS

Based on the ionic conduction phenomenon, the electro-thermo-convection (ETC) problem in non-Newtonian dielectric fluids is investigated in detail to serve as the active heat removal means with

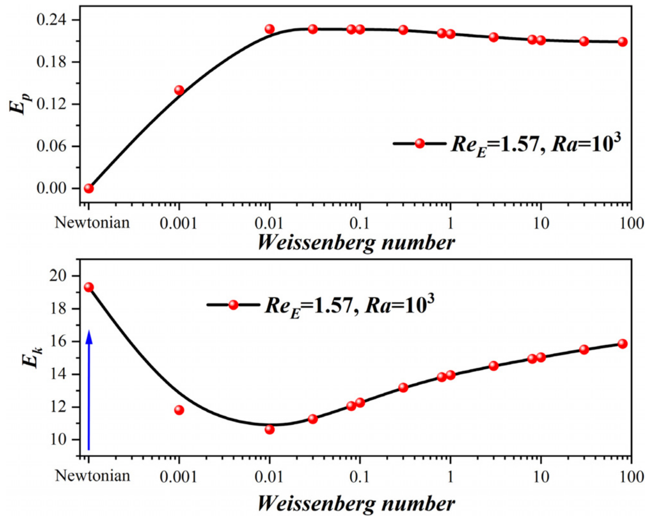

FIG. 12. The elastic energy (top) and kinetic energy (bottom) vs Weissenberg numbers. The fixed $Re_E=1.57$ and $Ra=10^3$.

complex fluid properties in microelectronic devices. The performance of heat transfer was evaluated with two differing configurations of gravity and electric fields (Config. 1 and Config. 2), where the shear-thinning and polymer elasticity are considered in our numerical implementation. The relevant results are summarized below:

The discrepancy in temperature profiles from pure RBCs is due to the different electroconvective patterns of ionically induced flow. The Nusselt number Nu and the ratio R_{ht} are used to elucidate the enhanced heat transfer of the ETC. Two significant partitions can be divided by the Rayleigh number Ra in Config. 1, namely, the thermal diffusion-dominated ($Ra \leq 10^3$) and the thermal convection-dominated regions ($Ra > 10^3$). In Config. 1, R_{ht} is enhanced at low Rayleigh numbers, with the maximum $R_{ht} = 13.9$ higher without electric field reinforcement. In the cooperative EC-RBC system, Nu proceeds through a linear increase, saturation, and a secondary rise for Config. 2. R_{ht} reaches a maximum of 5.02 times higher than that in the absence of EHD. Overall, Config. 1 (F_i in the same direction as gravity) allows higher heat transfer enhancement rates compared to Config. 2 (F_i in the opposite direction as gravity).

The rheological properties in ETC problems are also investigated in detail with polymer additions, including the elastic dependence (Wi) and shear thinning effects (α). With a rising α parameter, the temperature is more homogeneous, resulting from the main vortex (Mv) and secondary vortex (Sv) structure. Related findings indicate that the mobility factor has an optimistic impact on the flow rate and kinetic energy gains. In addition, a sharp surge of heat transfer is induced at $\alpha < 0.1$ and a lesser enhancement when $\alpha \geq 0.1$. Nu shows a 10% reduction (Config. 1) and a 5.5% reduction (Config. 2), respectively. The polymer absorbs kinetic energy from the flow field at low Wi numbers, resulting in a local reduction in the flow strength (kinetic energy). When surpassing the threshold $Wi_{cr} = 0.01$, Nu exhibits a rising stage with the recovery of kinetic energy. The R_{Nu} (the ratio of the viscoelastic Nu_V to the Newtonian Nu_0) can be modulated by polymer elasticity in a range of 14.5% (Config. 1), while it is only influenced within a range of 11% (Config. 2). A detailed evaluation of the force distributions reveals a noteworthy influence on fluid convection and energy inputs. Nonmonotonic curves of polymers on interfacial stress, buoyancy contribution, and convective strength, in turn, modifying heat transfer performances.

ACKNOWLEDGMENTS

This work is supported by the National Natural Science Foundation of China (Grant No. 52076055) and the Fundamental Research Funds for the Central Universities (Grant No. FRFCU5710094020). Numerical computations were performed at the Hefei Advanced Computing Center.

AUTHOR DECLARATIONS

Conflict of Interest

The authors have no conflicts to disclose.

Author Contributions

Di-Lin Chen: Investigation (equal); Methodology (equal); Validation (equal); Visualization (equal); Writing – original draft (equal). **Kang Luo:** Conceptualization (supporting); Project administration (equal); Software (equal). **Chun (Charles) Yang:** Software (equal); Supervision (equal); Writing – review & editing (equal). **Hong-Liang Yi:** Funding acquisition (lead); Supervision (lead).

DATA AVAILABILITY

The data that support the findings of this study are available from the corresponding author upon reasonable request.

APPENDIX A: BENCHMARK VALIDATION AND ASSOCIATED DATA

Here, the heat transfer strength Nu and kinetic energy E_k evolution curves with time are given first in Fig. 14.

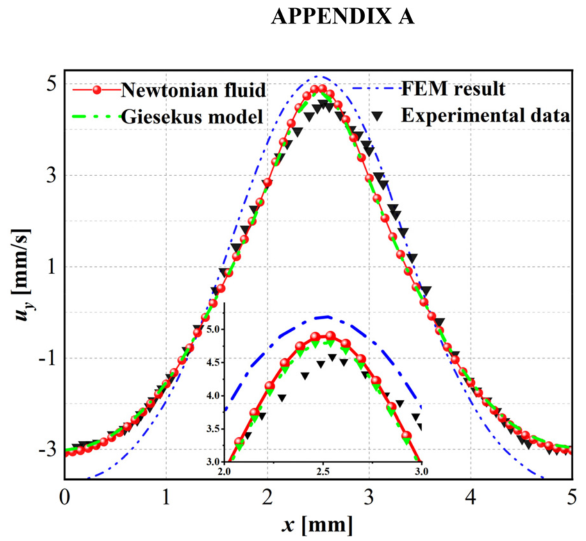

FIG. 13. Fitting curves of the numerical simulation results by the Giseskus model to Newtonian fluid and experimental data.

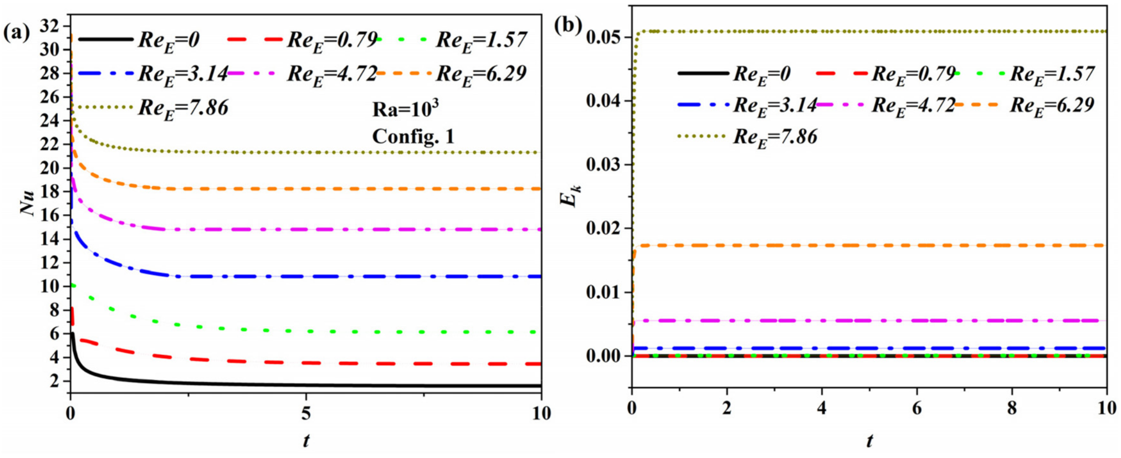

FIG. 14. (a) Evolutionary trend of the *Nu* number over time (dimensionless with Nu_0 in the absence of an electric field) and (b) kinetic energy evolution under ConFIG. 1.

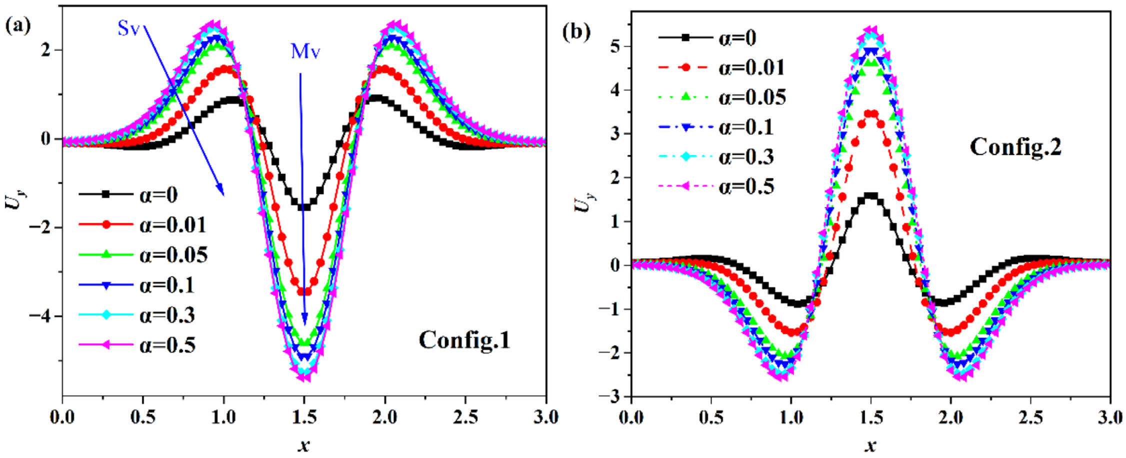

FIG. 15. Effect of shear thinning on the *y*-directional velocity U_y for two configurations: (a) Config. 1 and (b) Config. 2.

Furthermore, the velocity, streamline, and temperature distribution characteristics are displayed in Appendix A to clarify the reasons for the influences on the heat transfer properties. Figure 15 shows that the amplitude of U_y tends to be higher with an increasing α parameter for both config. 1 and 2. Although the two have a high degree of similarity, the *Nu* numbers are dramatically different in Fig. 8, depending on the internal flow structure and the electroconvection strength on the hot chips. Figure 15 shows that the position of the center of the primary vortex is invariant, but the amplitude and coverage expand. In contrast, the size of the secondary vortex decreases as α increases although it increases in amplitude. We show the structure of the main vortex (Mv) and secondary vortex (Sv) in Fig. 16. The gold dotted lines indicate the edges of the sidewall secondary vortices, showing the positive dependence of the Mv size and the negative interaction of the Sv size on α parameters.

APPENDIX B: OPERATING REGIMES FOR ION CONDUCTION FLOW

The EHD conduction phenomenon exists in two distinct types of operation regimes, which are distinguished by C_0,

$$C_0 = \frac{e_0 c_0 d^2}{\varepsilon \Delta\phi} = \frac{\sigma_0 d^2}{2\varepsilon K \Delta\phi} = \frac{d^2/(K\Delta\phi)}{\varepsilon/\sigma_0} = \frac{\tau_K}{2\tau_\sigma^0}. \tag{B1}$$

Ion transport time $t_K = d/KE_0$ denotes the time it takes for ions to drift from one electrode to the opposite electrode. The Ohmic time $t_\sigma^0 = \varepsilon/\sigma_0$ denotes the time during which dissolved ions are recombined to neutral species without an electric field. In the presence of an electric field-enhanced dissociation (Onsager–Wien effect),[33,40,63] the Ohmic time is adjustable:

$$\tau_\sigma = \varepsilon/\sigma = \tau_\sigma^0\sqrt{F(b)}, \quad \sigma = \sigma_0\sqrt{F(b)}, \quad F(b) = 1 + 2\beta^2 E^*/C_0, \tag{B2}$$

where σ_0 is the conductivity of the dielectric liquid without electric field action. Thus, the distance λ_H (an ion drifts from one electrode to the neutral volume for ionic recombination in response to an electric field) can be expressed as

$$\lambda_H \simeq KE_0\tau_\sigma^0 = \frac{d}{2C_0\sqrt{F(b)}} = \frac{d}{2C_0^E}. \tag{B3}$$

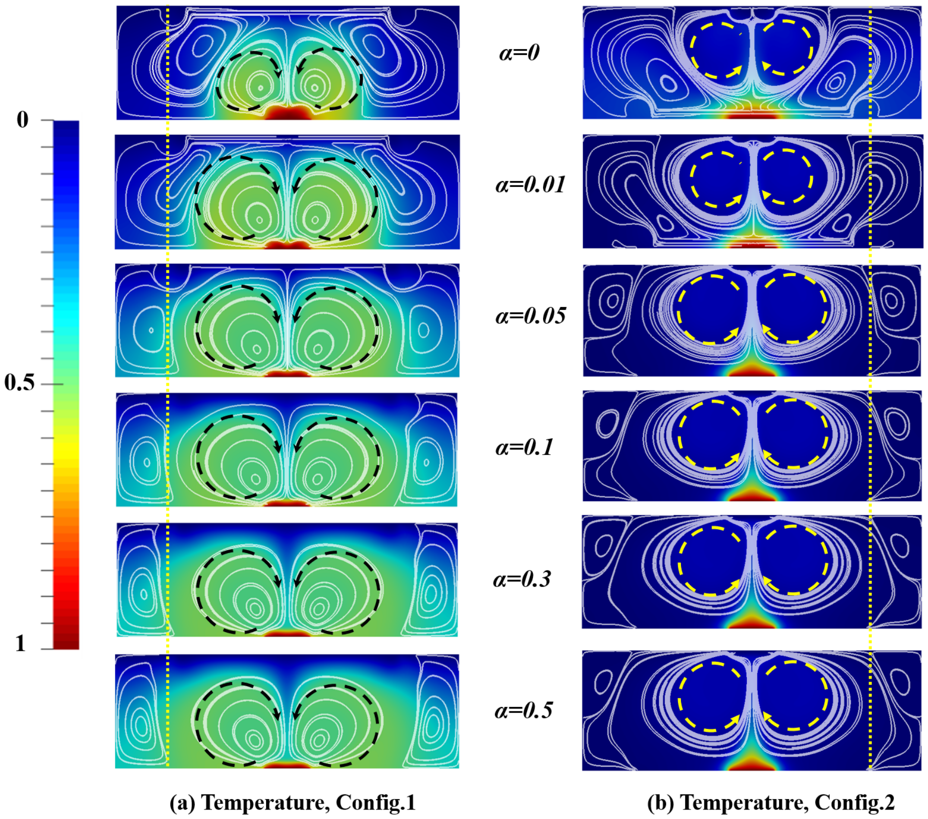

FIG. 16. The structure of the main vortex (Mv) and secondary vortex (Sv) for different α parameters with the temperature contours superimposed streamlines: (a) Config. 1 and (b) Config. 2.

Above, $F(b) = I_1(4b)/2b$ are known as the Onsager function, $C_0^E = C_0\sqrt{F(b)}$, and b represents the enhanced dissociation rate factor,

$$F(b) = \sum_{n=0}^{\infty} \frac{b^{2n}}{n!(n+1)!}. \tag{B4}$$

I_1 is the modified Bessel function of the first kind and order 1. b can be calculated by $b = l_B/l_o$, with the Bjerrum distance and the Onsager distance in Eq. (9). Therefore, the λ_H dimension relies upon the fluid nature and imposed electric field. The conduction mechanism acts on the saturation regime:

$$C_0 \ll 1, \quad \tau_0^\sigma \gg \tau_k, \quad \lambda_H \gg d. \tag{B5}$$

This indicates that the DSL overlaps without an electroneutral bulk. Conversely, the following relation exists:

$$C_0 \gg 1, \quad \tau_0^\sigma \ll \tau_k, \quad \lambda_H \ll d. \tag{B6}$$

This indicates that ions have time to recombine inside the bulk volume, so there are net charge densities $[\rho_E = e\ (c_+ - c_-)]$ in the bulk. Although we have carried out earlier on flow instability within a wide range of conduction numbers C_0, for the sake of simplifying the heat transfer analysis in this paper, we fix $C_0 = 59$. This is consistent with the setting $C_0 > 1$, accompanied by small DSL layer thicknesses in the vicinity of the electrodes, found in most of the experimental and numerical investigations.[1,5,6,15,37]

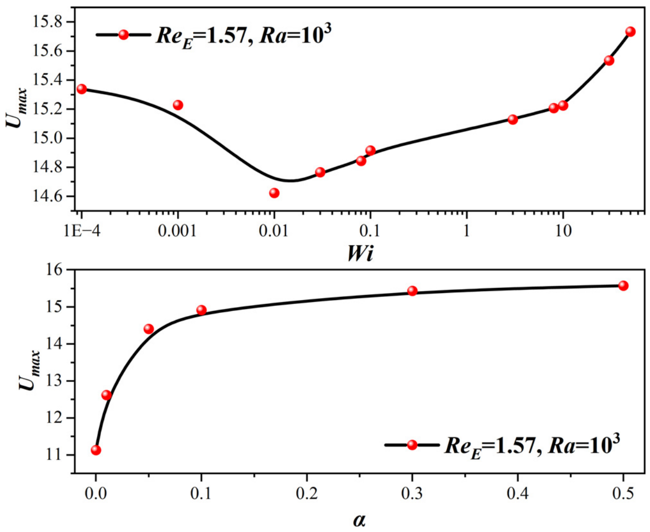

FIG. 17. Maximum velocity U_{max} trends within the flow field influenced by polymer elasticity (top) and shear-thinning (bottom).

REFERENCES

[1] M. Jafari, N. Farrokhi, and E. Esmaeilzadeh, "Effects of working temperature and fluid physical properties on heat transfer enhancement in conduction pumping: An experimental study," Int. J. Therm. Sci. **156**, 106471 (2020).

[2] Y.-Y. Bao, J.-H. Huang, Y.-J. Chen, and Z.-H. Liu, "Natural convection heat transfer of nanofluid in a cavity under an inhomogeneous electric field," Int. J. Heat Mass Transfer **131**, 341–345 (2019).

[3] A. I. Zhakin, "Electrohydrodynamics," Phys.-Usp. **55**, 465–488 (2012).

[4] V. Cacucciolo, H. Shigemune, M. Cianchetti, C. Laschi, and S. Maeda, "Conduction electrohydrodynamics with mobile electrodes: A novel actuation system for untethered robots," Adv. Sci. **4**, 1600495 (2017).

[5] V. Cacucciolo, J. Shintake, Y. Kuwajima, S. Maeda, D. Floreano, and H. Shea, "Stretchable pumps for soft machines," Nature **572**, 516–519 (2019).

[6] V. K. Patel and J. Seyed-Yagoobi, "Long-term performance evaluation of microscale two-phase heat transport device driven by EHD conduction," IEEE Trans. Ind. Appl. **50**, 3011–3016 (2014).

[7] Y. Guan and I. Novosselov, "Numerical analysis of electroconvection in cross-flow with unipolar charge injection," Phys. Rev. Fluids **4**, 103701 (2019).

[8] G. Hu, T. Albrow-Owen, X. Jin, A. Ali, Y. Hu, R. C. Howe, K. Shehzad, Z. Yang, X. Zhu, and R. I. Woodward, "Black phosphorus ink formulation for inkjet printing of optoelectronics and photonics," Nat. Commun. **8**, 278 (2017).

[9] M. Yu, K. H. Ahn, and S. J. Lee, "Design optimization of ink in electrohydrodynamic jet printing: Effect of viscoelasticity on the formation of Taylor cone jet," Mater. Des. **89**, 109–115 (2016).

[10] B. Malraison and P. Atten, "Chaotic behavior of instability due to unipolar ion injection in a dielectric liquid," Phys. Rev. Lett. **49**, 723–726 (1982).

[11] M. Yazdani and J. S. Yagoobi, "The effect of uni/bipolar charge injection on EHD conduction pumping," J. Electrost. **75**, 43–48 (2015).

[12] E. D. Fylladitakis, M. P. Theodoridis, and A. X. Moronis, "Review on the history, research, and applications of electrohydrodynamics," IEEE Trans. Plasma Sci. **42**, 358–375 (2014).

[13] S. I. Jeong, J. Seyed-Yagoobi, and P. Atten, "Theoretical/numerical study of electrohydrodynamic pumping through conduction phenomenon," IEEE Trans. Ind. Appl. **39**, 355–361 (2003).

[14] Z. Sun, P. Yang, K. Luo, and J. Wu, "Experimental investigation on the melting characteristics of n-octadecane with electric field inside macrocapsule," Int. J. Heat Mass Transfer **173**, 121238 (2021).

[15] R. Gharraei, M. Hemayatkhah, S. Baheri Islami, and E. Esmaeilzadeh, "An experimental investigation on the developing wavy falling film in the presence of electrohydrodynamic conduction phenomenon," Exp. Therm. Fluid Sci. **60**, 35–44 (2015).

[16] V. K. Patel and J. Seyed-Yagoobi, "Combined dielectrophoretic and electrohydrodynamic conduction pumping for enhancement of liquid film flow boiling," J. Heat Transfer **139**, 061502 (2017).

[17] Y. Lu, Q. Ren, T. Liu, S. L. Leung, V. Gau, J. C. Liao, C. L. Chan, and P. K. Wong, "Long-range electrothermal fluid motion in microfluidic systems," Int. J. Heat Mass Transfer **98**, 341–349 (2016).

[18] J. F. Zhang, S. Wang, M. J. Zeng, and Z. G. Qu, "Experimental and numerical investigation on flow characteristics of large cross-sectional ionic wind pump with multiple needles-to-mesh electrode," J. Fluids Eng. **141**, 031105 (2019).

[19] V. K. Patel and J. Seyed-Yagoobi, "A mesoscale electrohydrodynamic-driven two-phase flow heat transport device in circular geometry and in-tube boiling heat transfer coefficient under low mass flux," J. Heat Transfer **137**, 041504 (2015).

[20] M. R. Pearson and J. Seyed-Yagoobi, "Experimental study of EHD conduction pumping at the meso- and micro-scale," J. Electrost. **69**, 479–485 (2011).

[21] S. A. Vasilkov, K. D. Poluektova, and Y. K. Stishkov, "Experimental and numerical study of an electrohydrodynamic pump operating due to the field-enhanced dissociation near a dielectric barrier," Phys. Fluids **32**, 107102 (2020).

[22] D. A. Lanbaran and R. Taqizadeh, "Application of EHD combination and triangular blades to enhance the cooling rate of hot barriers," J. Electrost. **111**, 103555 (2021).

[23] C. Louste, P. Traore, P. A. Vazquez, and J. S. Yagoobi, "PIV flow measurements of conduction pumping flow created by nine pairs of asymmetric surface electrodes," in *20th International Conference on Dielectric Liquids (ICDL)* (IEEE, 2019).

[24] D. Fernandes, D. Cho, and Y. Suh, "Electrohydrodynamic flow of dielectric liquid around a wire electrode-effect of truncation of onsager function," IEEE Trans. Dielectr. Electr. Insul. **21**, 194–200 (2014).

[25] L. Yang, M. Talmor, B. C. Shaw, K. S. Minchev, C. Jiang, and J. Seyed-Yagoobi, "Flow distribution control in meso scale via electrohydrodynamic conduction pumping," IEEE Trans. Ind. Appl. **53**, 1431–1438 (2017).

[26] L. Yang, "Flow distribution control and thermal homogenization with EHD conduction pumping and experimental studies in pool boiling and internal condensation," Mech. Eng. (2017).

[27] M. Nishikawara and J. Yagoobi, "Experimental study of electrohydrodynamic conduction pumping embedded in micro-scale evaporator," in *Industry Applications Society Annual Meeting* (IEEE, 2020).

[28] N. J. O'Connor, P. N. Christidis, N. V. Tobar, M. Talmor, and J. Yagoobi, "Experimental study of flexible electrohydrodynamic conduction pumping for electronics cooling," J. Electron. Packag. **142**, 041105 (2020).

[29] V. Singhal and S. V. Garimella, "Induction electrohydrodynamics micropump for high heat flux cooling," Sens. Actuators A **134**, 650–659 (2007).

[30] N. Nourdanesh and E. Esmaeilzadeh, "Experimental study of heat transfer enhancement in electrohydrodynamic conduction pumping of liquid film using flush electrodes," Appl. Therm. Eng. **50**(1), 327–333 (2013).

[31] S. S. M. Golsefid, N. Amanifard, H. M. Deylami, and F. Dolati, "Numerical and experimental study on EHD heat transfer enhancement with Joule heating effect through a rectangular enclosure," Appl. Therm. Eng. **123**, 689–698 (2017).

[32] J. Wang, R. Fu, and X. Hu, "Experimental study on EHD heat transfer enhancement with a wire electrode between two divergent fins," Appl. Therm. Eng. **148**, 457–465 (2019).

[33] S. D. Cho, V. D. Fernandes, and K. Y. Suh, "Electrohydrodynamic flow of dielectric liquid around a wire electrode—Effect of truncation of onsager function," IEEE Trans. Dielectr. Electr. Insul. **21**, 194 (2014).

[34] W. Kim, J. C. Ryu, Y. K. Sun, and K. H. Kang, "Pumping of dielectric liquids using non-uniform-field induced electrohydrodynamic flow," Appl. Phys. Lett. **99**, 224102 (2011).

[35] Y. Suh and K. Baek, "Competition between the bulk and the dissociation layer in electrohydrodynamic flow of dielectric liquid around coplanar electrodes," Phys. Rev. E **87**, 023009 (2013).

[36] P. Traoré, C. Louste, U. Seth, P. A. Vazquez, and J. Yagoobi, *Numerical Investigation of EHD Pumping through Conduction Phenomenon in a Rectangular Channel* (IEEE, 2019).

[37] L. Wang, Z. Wei, T. Li, Z. Chai, and B. Shi, "A lattice Boltzmann modelling of electrohydrodynamic conduction phenomenon in dielectric liquids," Appl. Math. Modell. **95**, 361–378 (2021).

[38] Y. Feng and J. Seyed-Yagoobi, "Understanding of electrohydrodynamic conduction pumping phenomenon," Phys. Fluids **16**, 2432–2441 (2004).

[39] J. C. Ryu, H. J. Park, J. K. Park, and K. H. Kang, "New electrohydrodynamic flow caused by the onsager effect," Phys. Rev. Lett. **104**, 104502 (2010).

[40] P. A. Vázquez, M. Talmor, J. Seyed-Yagoobi, P. Traoré, and M. Yazdani, "In-depth description of electrohydrodynamic conduction pumping of dielectric liquids: Physical model and regime analysis," Phys. Fluids **31**, 113601 (2019).

[41] Z.-G. Su, T.-F. Li, K. Luo, J. Wu, and H.-L. Yi, "Electro-thermo-convection in non-Newtonian power-law fluids within rectangular enclosures," J. Non-Newtonian Fluid Mech. **288**, 104470 (2021).

[42] J. Zhou and I. Papautsky, "Viscoelastic microfluidics: Progress and challenges," Microsyst. Nanoeng. **6**, 113 (2020).

[43] S. S. Datta, A. M. Ardekani, P. E. Arratia, A. N. Beris, I. Bischofberger, G. H. McKinley, J. G. Eggers, J. E. López-Aguilar, S. M. Fielding, and A. Frishman, "Perspectives on viscoelastic flow instabilities and elastic turbulence," Phys. Rev. Fluids **7**, 080701 (2022).

[44] X.-B. Li, F.-C. Li, W.-H. Cai, H.-N. Zhang, and J.-C. Yang, "Very-low-Re chaotic motions of viscoelastic fluid and its unique applications in microfluidic devices: A review," Exp. Therm. Fluid Sci. **39**, 1–16 (2012).

[45] M. Y. Hwang, H. Mohammadigoushki, and S. J. Muller, "Flow of viscoelastic fluids around a sharp microfluidic bend: Role of wormlike micellar structure," Phys. Rev. Fluids **2**, 043303 (2017).

[46] S. H. Spiegelberg and G. H. Mckinley, "Stress relaxation and elastic decohesion of viscoelastic polymer solutions in extensional flow," J. Non-Newtonian Fluid Mech. **67**, 49–76 (1996).

[47] M. Alipanah, M. Hatami, and A. Ramiar, "Thermal and rheological investigation of non-Newtonian fluids in an induced-charge electroosmotic micromixer," Eur. J. Mech. B **88**, 178–190 (2021).

[48] F.-C. Li, Y. Kawaguchi, B. Yu, J.-J. Wei, and K. Hishida, "Experimental study of drag-reduction mechanism for a dilute surfactant solution flow," Int. J. Heat Mass Transfer **51**, 835–843 (2008).

[49] M. Khalid, V. Shankar, and G. Subramanian, "Continuous pathway between the elasto-inertial and elastic turbulent states in viscoelastic channel flow," Phys. Rev. Lett. **127**, 134502 (2021).
[50] G. Li, L. A. Archer, and D. L. Koch, "Electroconvection in a viscoelastic electrolyte," Phys. Rev. Lett. **122**, 124501 (2019).
[51] D. Zhang, A. J. Warren, G. Li, Z. Cheng, X. Han, Q. Zhao, X. Liu, Y. Deng, and L. A. Archer, "Electrodeposition of zinc in aqueous electrolytes containing high molecular weight polymers," Macromolecules **53**, 2694–2701 (2020).
[52] F. Pimenta and M. Alves, "Electro-elastic instabilities in cross-shaped microchannels," J. Non-Newtonian Fluid Mech. **259**, 61–77 (2018).
[53] S. H. Sadek, F. T. Pinho, and M. A. Alves, "Electro-elastic flow instabilities of viscoelastic fluids in contraction/expansion micro-geometries," J. Non-Newtonian Fluid Mech. **283**, 104293 (2020).
[54] G. Tomar, V. Shankar, A. Sharma, and G. Biswas, "Electrohydrodynamic instability of a confined viscoelastic liquid film," J. Non-Newtonian Fluid Mech. **143**, 120–130 (2007).
[55] M. A. Vakili, A. Sadeghi, and M. H. Saidi, "Pressure effects on electroosmotic flow of power-law fluids in rectangular microchannels," Theor. Comput. Fluid Dyn. **28**, 409–426 (2014).
[56] S. Yigit, C. Mcroberts, and N. Chakraborty, "Numerical investigation of laminar Rayleigh–Bénard convection of power-law fluids in square cross-sectional cylindrical annular enclosures," Int. Commun. Heat Mass Transfer **78**, 112–120 (2016).
[57] F. Li, S.-Y. Ke, X.-Y. Yin, and X.-Z. Yin, "Effect of finite conductivity on the nonlinear behaviour of an electrically charged viscoelastic liquid jet," J. Fluid Mech. **874**, 5–37 (2019).
[58] S. Waheed, S. Noreen, D. Tripathi, and D. C. Lu, "Electrothermal transport of third-order fluids regulated by peristaltic pumping," J Biol. Phys. **46**, 45–65 (2020).
[59] Z. G. Su, T. F. Li, K. Luo, and H. L. Yi, "Nonlinear behavior of electrohydrodynamic flow in viscoelastic fluids," Phys. Rev. Fluids **6**, 093701 (2021).
[60] M. Yazdani and J. Seyed-Yagoobi, "Effect of charge mobility on dielectric liquid flow driven by EHD conduction phenomenon," J. Electrost. **72**, 285–294 (2014).
[61] H. K. Jiang, Y. Zhang, Z. Y. Zhang, K. Luo, and H. L. Yi, "Instability and bifurcations of electro-thermo-convection in a tilted square cavity filled with dielectric liquid," Phys. Fluids **34**, 064116 (2022).
[62] D.-L. Chen, K. Luo, J. Wu, and H.-L. Yi, "Electrohydrodynamic conduction pumping of a viscoelastic dielectric fluid with the Onsager–Wien effect," Phys. Fluids **33**, 113101 (2021).
[63] D.-L. Chen, Y. Zhang, X.-L. Gao, K. Luo, J. Wu, and H.-L. Yi, "Electrohydrodynamic conduction phenomena of a viscoelastic dielectric fluid with electroelastic instability," Phys. Rev. Fluids **8**, 053702 (2023).
[64] S. A. Vasilkov, V. A. Chirkov, and Y. K. Stishkov, "Electrohydrodynamic flow caused by field-enhanced dissociation solely," Phys. Fluids **29**, 063601 (2017).
[65] R. Comminal, J. Spangenberg, and J. H. Hattel, "Robust simulations of viscoelastic flows at high Weissenberg numbers with the streamfunction/log-conformation formulation," J. Non-Newtonian Fluid Mech. **223**, 37–61 (2015).
[66] D.-L. Chen, X.-P. Luo, Z.-G. Su, K. Luo, and H.-L. Yi, "Thermal gradient and elastic dependence of induced charge electro-osmosis in viscoelastic fluids," Phys. Fluids **35**, 012008 (2023).
[67] S. Peng, J. Li, Y. Xiong, X. Xu, and P. Yu, "Numerical simulation of two-dimensional unsteady Giesekus flow over a circular cylinder," J. Non-Newtonian Fluid Mech. **294**, 104571 (2021).
[68] H. Giesekus, "Constitutive equations for polymer fluids based on the concept of configuration-dependent molecular mobility: A generalized mean-configuration model," J. Non-Newtonian Fluid Mech. **17**, 349–372 (1985).
[69] H. Giesekus, "A simple constitutive equation for polymer fluids based on the concept of deformation-dependent tensorial mobility," J. Non-Newtonian Fluid Mech. **11**, 69–109 (1982).
[70] R. B. Bird, R. C. Armstrong, and O. Hassager, *Dynamics of Polymeric Liquids*, Fluid Mechanics Vol. 1 (Wiley, New York, 1987).
[71] M. Mostafaiyan, K. Khodabandehlou, and F. Sharif, "Analysis of a viscoelastic fluid in an annulus using Giesekus model," J. Non-Newtonian Fluid Mech. **118**, 49–55 (2004).
[72] R. D. Selvakumar, D. Zhonglin, and J. Wu, "Heat transfer intensification by EHD conduction pumping for electronic cooling applications," Int. J. Heat Fluid Flow **95**, 108972 (2022).
[73] R. Fattal and R. Kupferman, "Time-dependent simulation of viscoelastic flows at high Weissenberg number using the log-conformation representation," J. Non-Newtonian Fluid Mech. **126**, 23–37 (2005).
[74] J.-P. Cheng, H.-N. Zhang, W.-H. Cai, S.-N. Li, and F.-C. Li, "Effect of polymer additives on heat transport and large-scale circulation in turbulent Rayleigh-Bénard convection," Phys. Rev. E **96**, 013111 (2017).